Journal of Hazardous Materials 422 (2022) 126771

Contents lists available at ScienceDirect

Journal of Hazardous Materials

journal homepage: www.elsevier.com/locate/jhazmat

Research Paper

Release of particulate matter from nano-enabled building materials (NEBMs) across their lifecycle: Potential occupational health and safety implications

Dilpreet Singh [a], Antonella Marrocco [a], Wendel Wohlleben [b], Hae-Ryung Park [c], Avantika R. Diwadkar [d], Blanca E. Himes [d], Quan Lu [e], David C. Christiani [a], Philip Demokritou [a,*]

[a] Center for Nanotechnology and Nanotoxicology, Harvard T.H. Chan School of Public Health, Harvard University, 665 Huntington Ave., Boston, MA 02115, USA
[b] BASF SE, Material Physics, 67056 Ludwigshafen, Germany
[c] Department of Environmental Medicine, School of Medicine and Dentistry, University of Rochester, NY 14642, USA
[d] Department of Biostatistics, Epidemiology and Informatics, University of Pennsylvania, Philadelphia, PA 19104, USA
[e] Molecular and Integrative Physiological Sciences, Department of Environmental Health, T.H. Chan School of Public Health, Harvard University, 665 Huntington Ave., Boston, MA 02115, USA

ARTICLE INFO

Editor: Dr. S Nan

Keywords:
Nanofiller
Engineered nanomaterials
Coatings
Insulations
Sanding
Incineration
UV-aging/weathering
Exposure and risk assessment

ABSTRACT

The present study investigates potential nanomaterial releases and occupational health risks across the lifecycle of nano-enabled building materials (NEBMs), namely, insulations and coatings. We utilized real-world degradation scenarios of a) sanding (mechanical), b) incineration (thermal), and c) accelerated UV-aging (environmental) followed by incineration. Extensive physicochemical characterization of the released lifecycle particulate matter (LCPM) was performed. The $LCPM_{2.5}$ aerosol size fraction was used to assess the acute biological, cytotoxic and inflammatory effects on Calu-3 human lung epithelial cells. RNA-Seq analysis of exposed cells was performed to assess potential for systemic disease. Findings indicated that release dynamics and characteristics of LCPM depended on both the NEBM composition and the degradation scenario(s). Incineration emitted a much higher nanoparticle number concentration than sanding (nearly 4 orders of magnitude), which did not change with prior UV-aging. Released nanofillers during sanding were largely part of the matrix

Abbreviations: NEBM, nano-enabled building material; LCPM, lifecycle particulate matter; ENM, engineered nanomaterial; NEP, nano-enabled product; TD, thermal decomposition; INEXS, Integrated Exposure Generation System; PM, particulate matter; CNT, carbon nanotubes; PAH, polycyclic aromatic hydrocarbons; ISO, International Organization for Standardization; PCM, physicochemical and morphological; NEC, nano-enabled coating; INS1/INS2, the two insulation materials investigated in this study; DPP, diketopyrrolopyrrole; ACR, acrylic-based coating; S/TEM-EDX, Scanning and Transmission Electron Microscopy with Energy-Dispersive X-ray Spectroscopy; BET, Brunauer-Emmett-Teller method; SSA, specific surface area; ICP-MS, Inductively Coupled Plasma Mass Spectrometry; XRD, X-Ray Powder Diffraction; XRF, X-Ray Fluorescence; XPS, X-ray Photoelectron Spectroscopy; HEPA, High Efficiency Particulate Air filter; SMPS, Scanning Mobility Particle Sizer; OPS, Optical Particle Sizer; CCI, Compact Cascade Impactor; PTFE, Polytetrafluoroethylene; PUF, Polyurethane foam; APS, Aerodynamic Particle Sizer; TGA, Thermogravimetric analysis; FTIR, Fourier Transform Infrared Spectroscopy; GC-MS, Gas chromatography-mass spectrometry; SEDD, Sampling, extraction, dispersion, and dosimetry methodology; EMEM, Eagle's Minimum Essential Medium; FBS, Fetal bovine serum; DLS, dynamic light scattering; MS-WF, mild steel welding fume particles; MPPD, Multiple Path Particle Dosimetry Model; LDH, Lactate dehydrogenase; PBS, Phosphate Buffered Saline; ROS, Reactive oxygen species; EGF, Epidermal Growth Factor; FGF, Fibroblast Growth Factor; G-CSF, Granulocyte-colony stimulating factor; GM-CSF, Granulocyte monocyte-colony stimulating factor; GRO, Growth-Related Oncogene; IFN, Interferon; IL, Interleukin; IP-10, Interferon γ-induced protein 10; MCP-1, Monocyte chemotactic protein 1; M-CSF, macrophage-colony stimulating factor; MDC, Macrophages derived chemokine; MIG, Monokine Induced by Gamma Interferon; MIP, Macrophage inflammatory protein; PDGF, Platelet Derived Growth Factor; RANTES, Regulated upon Activation, Normal T Cell Expressed and Secreted; TGF, Transforming Growth Factor; TNF, Tumor Necrosis Factor; VEGF, Vascular Endothelial Growth Factor; RNA-seq, RNA-sequencing; PCR, Polymerase Chain Reaction; RAVED, Reproducible Analysis and Validation of Expression Data; QC, quality control; STAR, Spliced Transcript Alignment to a Reference; UCSC, University of California, Santa Cruz; GSEA, Gene Set Enrichment Analysis; KEGG, Kyoto Encyclopedia of Genes and Genomes; MSigDB, Molecular Signatures Database; AIM, Molecular Signatures Database 1; ANOVA, Analysis of Variance; MSDS, material safety data sheet; PAMS, poly(α-methylstyrene); PdI, polydispersity index; NES, normalized enrichment score; PE, polyethylene; PP, polypropylene; PC, polycarbonate; EVA, ethyl-vinyl acetate; PET, polyethylene terephthalate; IPF, idiopathic pulmonary fibrosis; PEL, permissible exposure limit; REL, recommended exposure limit; OSHA, Occupational Safety and Health Administration; NIOSH, National Institute for Occupational Safety and Health.

* Correspondence to: Department of Environmental Health, Center for Nanotechnology and Nanotoxicology, Harvard T.H. Chan School of Public Health, 665 Huntington Ave, Building 1, Room 1310, Boston, MA 02115, USA,.

E-mail address: pdemokri@hsph.harvard.edu (P. Demokritou).

https://doi.org/10.1016/j.jhazmat.2021.126771
Received 23 April 2021; Received in revised form 20 July 2021; Accepted 26 July 2021
Available online 29 July 2021

fragments, whereas those during incineration were likely physicochemically transformed. The LCPM from incineration showed higher bioactivity and inflammogenicity compared to sanding or sequential UV-aging and incineration, and more so when metallic nanofillers were present (such as Fe_2O_3). Overall, the study highlights the need for considering real-world exposure and toxicological data across the NEBM lifecycle to perform adequate risk assessments and to ensure workplace health and safety.

1. Introduction

Nanotechnology applications are rapidly increasing across the industrial and consumer sectors (Eleftheriadou et al., 2017; Xu et al., 2020; Aytac et al., 2020; Vaze et al., 2019; Pirela et al., 2017; Pyrgiotakis et al., 2016) with a significant fraction invested in the building and construction industry to enhance material properties, conserve energy expenditure and incorporate greener and environmentally sustainable structural materials (Lux Research, 2014; Lee et al., 2010). Applications of nano-enabled building materials (NEBMs) include but are not limited to paints and coatings (Lee et al., 2010; Hayashi et al., 1993; Kaiser et al., 2013), insulation materials (Rostam et al., 2015; Gao et al., 2014), flame retardants (Mosurkal et al., 2008), thermoplastic components (Saba et al., 2014), and multifunctional concrete and glass structures (Das and Mitra, 2014; Santosh and Madhavi, 2015; Jones et al., 2016), and incorporate a wide variety of engineered nanomaterials (ENMs) (Al-Bayati and Al-Zubaidi, 2018). It has been forecasted that the global value of nano-enabled products (NEPs), nano-intermediates, and nanomaterials will reach US$ 125 billion by 2024 (Lux Research, 2014).

Although the economic value and the societal benefit of nanotechnology in the construction sector are immense, very little is known about potential exposures to ENMs that may occur over the useful lifecycle of NEBMs. Occupational workers engaged in various construction/renovation/demolition-related activities may be exposed to aerosolized particulate matter (dust) released from the destructive manipulation of the NEBMs, a significant fraction of which may be inhalable and may contain the ENMs originally embedded in the NEBM matrices (Lee et al., 2010). These released LCPM (lifecycle-associated particulate matter) particles can be generated from various lysis scenarios that NEBMs might go through during their use or end-of-life disposal phase, such as mechanical degradation (sanding, drilling, cutting, grinding, etc.), thermal degradation (incineration, combustion during accidental fires, etc.) and environmental degradation (exposure to sunlight, rain, ambient temperature fluctuations, etc.) (Bello et al., 2013; Kang et al., 2017; Sung et al., 2014; Jacobs et al., 2016; Wohlleben et al., 2011; Koponen et al., 2011; Gomez et al., 2014; Golanski et al., 2011; Han et al., 2018; Wohlleben and Neubauer, 2016; Koivisto et al., 2017; Vorbau et al., 2009). The released LCPM may be a combination of pure matrix fragments, ENMs embedded or protruding from matrix fragments, and freely released ENMs that may have been significantly physicochemically transformed during the lysis scenario(s). In addition, LCPM particles may be accompanied by the release of several gaseous species and semi-volatile organic co-pollutants adsorbed to PM, depending on the specific lifecycle scenario, such as during thermal decomposition (TD) (Singh et al., 2017; Pirela et al., 2015; Chalbot et al., 2017). A significant fraction of the LCPM may be inhalable fine particles ($PM_{2.5}$) containing a mixture of carbonaceous and metallic species, with potential for adverse environmental health implications (Kermani et al., 2021).

Major knowledge gaps exist with respect to understanding exposures across the lifecycle of NEBMs, release mechanisms, and the properties of released LCPM. Both public health risk assessors and the industry are struggling with the fact that most of the ENM hazard data focus on pristine (raw) ENMs rather than impacts associated with worker/consumer use of NEPs, their disposal, and potential ENM release and transformations across the lifecycle (Grassian et al., 2016). This knowledge gap is highlighted in the latest National Institute for Occupational Safety and Health (NIOSH) Nanotechnology Research Plan for FY2018-25, where one of the strategic goals is to characterize emissions and particles generated from NEPs and evaluate their acute and chronic toxicity during workplace scenarios such as cutting, grinding, sanding, and spraying (Hodson et al., 2019). Importantly, there is a lack of exposure data assessing the LCPM release profiles across the lifecycle of NEBMs and critically, to answer the question of nano-related occupational health and safety risks to the workers involved in handling, usage, technical manipulation, and disposal of the NEBMs.

Recently, to address the lack of standardized methodologies and exposure generation platforms to investigate the end-of-life scenario via TD of NEPs, we developed a versatile Integrated Exposure Generation System (INEXS) (Sotiriou et al., 2015) that enables controlled parametric studies under different TD operational conditions such as the final temperature, heating rate, oxygen concentration and aerosol residence time. The INEXS platform was recently used to investigate the TD of several industrially-relevant thermoplastic nanocomposites and nanocoatings, widely used in the built environment (Singh et al., 2017, 2016, 2019a; Sotiriou et al., 2016; Watson-Wright et al., 2017). Interestingly, it was observed that the matrix-embedded inorganic nanofillers such as iron oxide (Fe_2O_3) and titanium dioxide (TiO_2) were released in trace amounts in the aerosol PM but the carbonaceous nanofillers such as CNTs (carbon nanotubes) were completely combusted at high TD temperatures. The released LCPM physicochemical properties, such as the mean aerosol size and the overall chemical composition, were strongly influenced by the NEP matrix and modulated by the nanofiller chemistry and weight loading in the matrix. The dominant fraction of the TD LCPM particles consisted of organic carbonaceous compounds (>99 wt%). The bulk of the inorganic nanofiller mass (>99%) was retained in the residual ash as agglomerated nanoparticles. We observed synergistic chemical interactions between the released inorganic nanofillers (such as Fe_2O_3) and the semi-volatile polycyclic aromatic hydrocarbon (PAH) co-pollutants (byproducts of combustion) to form higher molecular weight and more toxic and carcinogenic PAHs, illustrating nanofiller-specific effects on released LCPM chemistries and hence potential environmental health implications. The bioactivity and cytotoxicity of the released LCPM were found to be significantly associated with both the host polymer matrix and the nanofiller chemical composition.

In this study, the main objective was to investigate the potential occupational health and safety implications of an industrially relevant panel of NEBMs consisting of in-house synthesized nano-enabled acrylic-based coatings with inorganic or organic nanofillers, and commercially procured nano-enabled insulation materials. Three distinct categories of lifecycle lysis scenarios were used: a) sanding (a form of mechanical degradation representing the NEBM use phase during the lifecycle), using an existing standardized sanding platform (Neubauer et al., 2017), b) incineration (or thermal degradation) under standard industrial waste incinerator conditions (representing the NEBM end-of-life/disposal phase), utilizing our recently developed INEXS platform (Sotiriou et al., 2015), and c) accelerated UV-aging (simulating outdoor environmental weathering over several years) in an ISO (International Organization for Standardization)-standardized UV-exposure chamber (Wohlleben and Neubauer, 2016), followed by incineration in the INEXS platform. The roles of the NEBM matrix/-embedded nanofillers and the specific lifecycle degradation scenario(s) in determining the released LCPM dynamics and physicochemical/morphological (PCM) properties and potential acute toxicological implications were assessed. The novelty of our study lies in the

utilization of NEBMs of direct industrial relevance and application for the various realistic lifecycle degradation and occupational exposure scenarios in which workers may be exposed to unintentionally released LCPM. More importantly, the synergistic effects of combined, sequential lysis scenarios resembling real-world disintegration of NEBMs such as environmental (UV) aging over a lifetime followed by thermal degradation at the end-of-life on nanofiller release dynamics and subsequent occupational health risks were assessed.

2. Materials and methods

2.1. Panel of NEBMs

Table 1 summarizes the list of industrially relevant NEBMs that were utilized for our lifecycle investigations, along with their known chemical compositions. The panel consists of two families of NEBMs, namely, nano-enabled coatings (NECs) that were synthesized in-house and two commercially available insulation blankets that were provided in-kind through a local construction workers' union (code-named for anonymity: INS1 and INS2). The NECs consisted of an acrylic copolymer matrix containing an alumina-passivated non-nano white TiO_2 pigment in a defined proportion and the nanofiller at a defined weight loading, which was then applied on a pure quartz substrate at ~100 μm thickness. Two different kinds of nanofillers were utilized, each at 1.5 wt% loading in the coating matrix, namely, Fe_2O_3 (iron oxide) and DPP-Red (organic pigment of the chemical substance diketopyrrolopyrrole). A coating with an identical matrix but without any nanofiller was also formulated to act as the control coating for all NECs. The corresponding assigned codes for the coatings were ACR, Fe-ACR, and DPP-ACR. Technical details on the synthesis of the NECs have been provided in the Supporting Information **(SI)** file. The corresponding codes for the generated $LCPM_{2.5}$ (aerodynamic size fraction less than 2.5 μm) from the insulations and coatings during the different lifecycle scenarios were assigned by prefixing the appropriate symbol before the NEBM code name (last column in Table 1), i.e., "M" for mechanical degradation (sanding), "I" for incineration, and "UV" for aging by UV light exposure.

2.2. PCM characterization of NEBMs

2.2.1. Nanofillers in NECs

Detailed PCM characterization of the Fe_2O_3 and DPP-Red nanofillers used in the synthesis of NECs was conducted using a variety of analytical techniques such as scanning and transmission electron microscopy with energy-dispersive X-ray spectroscopy (S/TEM-EDX) to assess nanofiller morphology, size, and surface elemental composition; Brunauer-Emmett-Teller (BET) method to measure nanofiller specific surface area (SSA); inductively coupled plasma mass spectrometry (ICP-MS) to measure elemental concentrations in the nanofiller; X-ray powder diffraction (XRD) to assess crystallinity and purity of the nanofiller; X-ray fluorescence (XRF) for bulk elemental analysis of the nanofiller; and X-ray photoelectron spectroscopy (XPS) to determine surface elemental composition. Further characterization details are described in the **SI.**

2.2.2. PCM characterization of pristine insulation materials

In order to address the critical question of whether the commercially procured insulations are indeed nano-enabled, extensive PCM characterization was performed. Small rectangular sections of the materials across the entire thickness of the insulation blankets were cut out to prepare samples for analysis. The morphology and surface elemental composition were assessed through SEM/TEM/EDX to look for the presence of nanoparticles and their surface chemical composition, and the bulk elemental composition of the insulations was quantified with ICP-MS.

2.3. Lifecycle degradation scenarios investigated on NEBMs

2.3.1. Sanding

The two insulations were mechanically degraded in a sanding setup described in detail in Neubauer et al (Neubauer et al., 2017). Fig. S1 shows the schematic of the sanding chamber setup. Briefly, sanding on the insulation blankets was conducted inside a 0.15 m^3 aerosol chamber equipped with a drilling machine (Bosch, GBS 21-2 RCT Professional) and flushed by particle-free air from a HEPA (High Efficiency Particulate Air) filter before the experiment. The drilling head was equipped with a sanding support (disc of diameter 115 mm, sanding paper with grit size 80, Starcke GmbH & Co.KG). The insulation sheets to be investigated

Table 1
List of NEBMs utilized in the study – family (source), material code, material description, composition, investigated lifecycle scenarios and released $LCPM_{2.5}$ code.

Family of building material	Material Code	Material Description	Composition	Lifecycle scenarios investigated	Released LCPM Code
Coatings (source: Synthesized at BASF labs, Germany)	ACR	Acrylic polymer-based matrix (applied on pure quartz substrate at ~100 μm thickness)	Matrix = Acrylic (~52–53 wt%) + alumina-passivated non-nano TiO_2 pigment (~42–43 wt%)	Incineration UV-Aging followed by Incineration	I_ACR I_UV_ACR
	Fe(s)-ACR	Acrylic matrix with iron oxide nanofiller	Matrix + 1.5 wt% Fe_2O_3 nanofiller of mean size ~37 nm	Incineration UV-Aging followed by Incineration	I_Fe(s)-ACR I_UV_Fe(s)-ACR
	Fe(L)-ACR	Acrylic matrix with iron oxide nanofiller	Matrix + 1.5 wt% Fe_2O_3 nanofiller of mean size ~150 nm	Incineration	I_Fe(L)-ACR
	DPP-ACR	Acrylic matrix with[a]DPP-Red organic nanofiller	Matrix + 1.5 wt% DPP-Red nanofiller of mean size ~43 nm	Incineration UV-Aging followed by Incineration	I_DPP-ACR I_UV_DPP-ACR
Insulations (source: local construction workers union in Boston, MA)	INS1	Cryogenic insulation blanket	[b]Trimethylated Silica (40–50%), Fibrous Glass (10–20%), Polyethylene Terephthalate (10–20%), Magnesium Hydroxide (<5%), Aluminum (<5%)	Sanding Incineration	M_INS1 I_INS1
	INS2	High-temperature insulation blanket	[b]Trimethylated Silica (40–50%), Fibrous glass (textile grade) (40–50%), Titanium Dioxide (1–5%), Aluminum Trihydrate (1–5%)	Sanding Incineration	M_INS2 I_INS2[c]

[a] DPP Red (aka Pigment Red 254): Organic pigment with an IUPAC name of 3,6-bis(4-chlorophenyl)− 2,5-dihydropyrrolo[3,4-*c*]pyrrole-1,4-dione, molecular formula $C_{18}H_{10}Cl_2N_2O_2$ and CAS No. 84632–65–5

[b] Obtained from the material safety data sheet (MSDS) provided by the manufacturer

[c] Negligible $PM_{2.5}$ collected due to lack of thermal degradation of the material, even at temperatures higher than 850 °C

were mounted onto a fixed holder which did not rotate during the experiments. A contact force of 17 N was applied by using a spring with a diameter of 4 mm. The rotational frequency of the disc was maintained at 1330 rpm during each sanding operation that lasted 60 s. Triplicate sanding experiments were performed for each insulation. The real-time monitoring of the concentration and size of the released aerosol was performed using the TSI SMPS 3080 (Scanning Mobility Particle Sizer), allowing detection and quantification of airborne nanoparticles between 10 nm and 300 nm. Furthermore, the released aerosol was monitored using the TSI OPS 3330 (Optical Particle Sizer), allowing for size-resolved quantification of larger particles between 0.3 and 10 μm. The released particles were sampled onto gold filters (APC, 25 mm diameter, 0.2 μm pore size) for subsequent SEM/EDX analysis. The chamber was kept closed during the whole experiment. After sanding, the collected dusts at the bottom of the chamber were retrieved and stored in plastic containers. It is worth noting that the sandpaper abrasive was silicon carbide, which is an extremely hard material (compared to the soft insulation blankets) and contains no metals. Therefore, it is not expected to degrade and release particles during sanding and hence interfere in the elemental analysis of the sanded dusts.

The size fractionation of the collected sanded dusts was done by re-aerosolization of the dusts using the TSI Fluidized Bed Aerosol Generator 3400 A (Fig. S2) followed by collection of the $PM_{2.5}$ size fraction using the 30 L/min Harvard Compact Cascade Impactor (CCI), as described previously (Demokritou et al., 2004). The bead purge flow in the fluidized bed was adjusted to 2 L/min and the bed flow to 15 L/min. The sampling was performed for at least 2–3 h in order to collect at least a few mg of $PM_{2.5}$ for PCM and toxicological characterization. The $PM_{2.5}$ size fraction was collected on PTFE (Polytetrafluoroethylene or Teflon) membrane disc filters (47 mm diameter, 2 μm pore size, Pall Corporation, NY). The $PM_{>2.5}$ size fraction was collected on rectangular polyurethane foam (PUF) substrates. Gravimetric analysis of the collected size fractions ($PM_{2.5}$ and $PM_{>2.5}$) was performed to obtain the mass-size distributions of the aerosolized sanded PM from the insulations. During size-fractionated sampling, the aerosol number concentration and particle size distribution were also measured using the TSI APS 3321 (Aerodynamic Particle Sizer).

2.3.2. UV-aging

Three coatings (as applied on quartz substrates), namely, ACR, Fe(s)-ACR, and DPP-ACR were weathered under ISO4892 standardized aging protocol with 60 W/cm^2 UV intensity (integrated across the wavelength range of 300–400 nm) (ISO, 2021). The specimen aging was performed in a stand-alone equipment (Suntest XLS+), where the specimens were covered by a UV-transparent borosilicate glass to prevent any loss of fragments for a period of 3 months, which roughly corresponds to two years of outdoor weathering (Wohlleben and Neubauer, 2016). The weathering was performed on triplicate coating samples for each coating type.

2.3.3. Incineration

The coatings (pristine and UV-aged) and the insulations were thermally decomposed using the INEXS platform (Sotiriou et al., 2015) (Fig. S3) at the standard incineration conditions, i.e., 850 °C, 20.9 vol% O_2, and a heating rate of 20 °C/min starting from room temperature. The maximum temperature was reached in 40 min and was held constant for 10 min to ensure maximum degradation, resulting in a total 50 min of incineration time. The mass of each coating incinerated was ~100 mg whereas ~500 mg each of the insulations was used for incineration. A higher amount is used for the insulations due to a higher amount of incombustible metal content of the insulations to collect enough released particles for PCM and toxicological analysis. The released aerosol during TD was monitored in real-time using the TSI SMPS 3080 for the concentration and size of nanoparticles (~5–300 nm mobility size) and using the TSI APS 3321 for the larger particles (0.5–20 μm aerodynamic size). The released aerosol was also size-fractionated and collected in the Harvard CCI (Demokritou et al., 2004) throughout the incineration time (50 min) to collect the $PM_{2.5}$ aerodynamic size fraction on Teflon membrane disc filters for further PCM and toxicological characterization. Gravimetric analysis of the collected size fractions ($PM_{2.5}$ and $PM_{>2.5}$) was performed to obtain the mass-size distributions of the incineration PM from the coatings and insulations. The amount of residual ash remaining after incineration was weighed after each experiment to calculate the residual ash yields (mass %) from the coatings and insulations.

2.4. PCM characterization of released LCPM

2.4.1. Sanding LCPM

The bulk size sanding dusts from insulations collected on the gold filters were analyzed for shape and surface elemental composition using SEM/EDX and TEM to detect the presence of released nanoscale fragments and their composition. Furthermore, the collected insulation dusts were analyzed for the quantitative mass concentration of 55 elements (metals/non-metals) using ICP-MS to determine their bulk elemental composition. Further details on ICP-MS are described in the **SI** text.

2.4.2. Incineration LCPM

The collected $PM_{2.5}$ size fraction during incineration of coatings and insulations was analyzed for the concentration of 55 elements (metals/non-metals) using ICP-MS to determine the quantitative release of metals in the LCPM. To assess the release of the organic nanofiller DPP-Red, XPS analysis was performed on the incineration $PM_{2.5}$ from the DPP-Red containing coatings to look for chlorine (Cl), the unique characteristic element in the DPP-Red molecule ($C_{18}H_{10}Cl_2N_2O_2$). Further details are described in the **SI** text.

In addition, to assess the chemical composition of the evolved gaseous species during the thermal decomposition of the insulation materials, thermogravimetric analysis (TGA) (NETZSCH TG 209 F1 Libra) coupled with Fourier transform infrared spectroscopy (FTIR) and gas chromatography-mass spectrometry (GC-MS) was employed. Further details on this analysis are described in the **SI** text.

2.5. LCPM extraction and colloidal characterization

The sanding and incineration $LCPM_{2.5}$ collected on Teflon filters in the CCI was extracted into a concentrated aqueous stock suspension using the previously developed SEDD (sampling, extraction, dispersion, and dosimetry) methodology by the authors (Pal et al., 2015). A dispersion of the LCPM in water was then achieved by delivering the critical sonication energy to the suspension to reduce the agglomerate size, per previously established dispersion protocols (Cohen et al., 2014; DeLoid et al., 2016). Dispersed stock solutions in deionized endotoxin-free water were diluted to 100 μg/mL in the EMEM (Eagle's Minimum Essential Medium) + 10% FBS (fetal bovine serum) cellular media and vortexed for 30 s. LCPM suspensions in pure water and cellular media were then characterized for various colloidal parameters using dynamic light scattering (DLS, Malvern Zetasizer Nano ZS), which provides the intensity-averaged hydrodynamic diameter, zeta potential, polydispersity index, and specific conductance of the particles in suspension.

2.6. Cell culture and exposure

As inhalation exposures of the workers to the released LCPM from NEBMs are a concern in the occupational setting, the human lung epithelial cell line Calu-3 purchased from the American Type Culture Collection (ATCC HTB-55, Manassas, VA) was used and cultured in EMEM culture media (ATCC, Manassas, VA), supplemented with 10% (FBS), 100 U/mL of penicillin G and 100 μg/mL streptomycin and grown at 37 °C in 5% CO_2.

Cells were seeded in 96 or 24 well plates at a density of 0.5×10^6 cells/mL in 100 μL or 600 μL growth medium for a single well of a 96 or 24-well plate respectively and were treated for 24 h. Two administered doses of the LCPM were utilized for the basic cytotoxicity assays (20 and 75 μg/mL), whereas the higher dose of 75 μg/mL was administered for the acute inflammatory biomarker assessment. The selected cellular doses were derived from experimentally obtained LCPM exposure data and simulation of lung-deposited LCPM dose using the Multiple Path Particle Dosimetry Model (MPPD, v3.04) (Anjilvel, 1995; Cassee et al., 1999; Miller et al., 2016) (calculation details described in the SI). Appropriate controls, including culture medium and the LCPM dispersion vehicle control, and the comparator material mild steel welding fume (MS-WF) particles (obtained from Dr. J.M. Antonini, NIOSH) were utilized in all cellular toxicological experiments. MS-WF particles, with a count mean diameter of 1.22 μm, were generated as described previously (Antonini et al., 1999, 2012). Cellular exposures of all LCPM materials and controls were performed in at least triplicates (triplicate administered doses to cells) in order to be able to perform a robust statistical analysis of the observed cellular responses.

2.7. Cell viability assay

Lactate dehydrogenase (LDH) in the supernatant of 24 h treated cells in a 96-well plate was measured using the Pierce LDH assay kit (Sigma Aldrich, St. Louis, MO, USA) according to the manufacturer's instructions. Untreated cells were used to measure spontaneous LDH release and lysed cells, using 150 μL 10X lysis buffer 45 min prior to the end of incubation, were used to measure maximum LDH release. Apical supernatant from each well was transferred to a 1.5 mL tube and 50 μL of supernatant from each tube was then added in triplicate wells in a new 96-well plate. Fifty μL of the reaction mixture was added and mixed using a multichannel pipette. Plates were incubated at room temperature for up to 30 min protected from light, and the reaction was stopped by adding 50 μL of stop solution. Absorbance was measured at 490 nm (A_{490}) and 680 nm (A_{680}). To calculate LDH activity, A_{680} values were subtracted from A_{490} values to correct for instrument background. To correct for particle/medium interference/background, LDH activities from no-cell controls were subtracted from test well LDH activities. Percent cytotoxicity was calculated by subtracting spontaneous LDH release values from treatment values, dividing by total LDH activity (Maximum LDH activity – Spontaneous LDH activity), and multiplying by 100.

2.8. Metabolic activity assay

PrestoBlue metabolic activity (cell viability) assay was performed after 24 h exposure using cells cultured and exposed in a 96-well plate. PrestoBlue® cell viability reagent (ThermoFisher Scientific, Waltham, MA, USA) was used according to the manufacturer's instructions. Cells treated with lysis buffer for 1 h at 37 °C were used as positive controls for inhibition of metabolic activity. Briefly, the supernatant was removed from each test wells, the wells were washed 3 times with 300 μL of PBS (Phosphate Buffered Saline) and 100 μL of 10% PrestoBlue reagent was added to each test well. Plates were then incubated at 37 °C for 15 min, and fluorescence was measured at 560 nm (excitation)/590 nm (emission). Percent metabolic activity was reported as normalized on the response from the negative control/untreated cells (100%).

2.9. Oxidative stress/reactive oxygen species (ROS) assay

ROS analysis was performed after 6 h treatment in a 96-well plate. Production of ROS was assessed using the CellROX® green reagent (Thermo Fisher Scientific, Waltham, MA, USA) according to the manufacturer's instructions. Cells treated with 100 μM menadione for 1 h at 37 °C were used as positive controls for ROS generation. Briefly, media was removed from each test well, the wells were washed 3 times with 200 μL PBS, 100 μL of working solution (CellROX Reagent) was added in each well, and plates were incubated for 30 min at 37 °C. The supernatant was removed, and wells were then washed 3 times with 200 μL PBS. Fluorescence was measured at 480 nm (excitation)/520 nm (emission). Percent ROS generation was reported as normalized on the maximum ROS generation from the positive control as 100%.

2.10. Inflammatory response assessment

The supernatants from cells exposed to the higher dose (75 μg/mL) LCPM for 24 h were collected and shipped on dry ice for cytokine and chemokine assessment using the Human Cytokine Array / Chemokine Array 48-Plex (HD48) assay (Eve Technologies, Calgary, AB). The samples were prepared according to Eve Technologies' protocol. Briefly, the supernatants from each well were transferred in new 1.5 mL tubes, centrifuged at 3000 x g for 10 min to remove debris, and transferred to a new 1.5 mL tube. Then 75 μL of supernatant from each sample were aliquoted in new 0.5 mL tubes and stored at − 80 °C until shipment. The remaining supernatant was aliquoted and frozen at − 80 °C for additional experiments.

The 48-plex consisted of soluble CD40 ligand (sCD40L), Epidermal Growth Factor (EGF), Eotaxin, Fibroblast Growth Factor (FGF-2), FMS-like tyrosine kinase 3 ligand (Flt-3L), Fractalkine, granulocyte-colony stimulating factor (G-CSF), granulocyte monocyte-colony stimulating factor (GM-CSF), Growth-Related Oncogene (GRO)-α, Interferon (IFN)-α2, Interferon gamma (IFNγ), Interleukin-1α (IL-1α), IL-1ra, IL-1β, IL-2, IL-3, IL-4, IL-5, IL-6, IL-7, IL-9, IL-10, IL-12 (p40), IL-12 (p70), IL-13, IL-15, IL-17A, IL-17E, IL-17F, IL-18, IL-22, IL-27, IFN-γ-inducible protein 10 (IP-10), monocyte chemotactic protein 1 (MCP-1/CCL2), MCP-3, macrophage- colony stimulating factor (M-CSF), Macrophages derived chemokine (MDC/CCL22), monokine induced by gamma interferon (MIG), macrophage inflammatory protein 1α (MIP-1α), MIP-1β, Platelet derived Growth Factor (PDGF)-AA, PDGF-AB/BB, Regulated on Activation, Normal T-cell Expressed and Secreted (RANTES), Transforming growth Factor (TGF)-α, tumor necrosis factor α (TNFα), TNFβ and vascular endothelial growth factor (VEGF)-A.

2.11. RNA-Seq transcriptomic profiling

Total RNA was extracted from the higher dose (75 μg/mL) LCPM-exposed cells after 24 h using the miRNeasy kit (Qiagen) according to the manufacturer's instructions and used for RNA-Seq transcriptional profiling to detect broad toxicological effects of LCPM exposure and possible systemic disease mechanisms at play. Three samples for each LCPM exposure group were obtained.

2.11.1. RNA-Seq library preparation and sequencing

Polyadenylated mRNAs were selected from total RNA samples using oligo-dT-conjugated magnetic beads on an Apollo324 automated workstation (PrepX PolyA mRNA isolation kit, Takara Bio USA). Entire poly-adenylated RNA samples were immediately converted into stranded Illumina sequencing libraries using 200 bp fragmentation and sequential adapter addition on an Apollo324 automated workstation following manufacturer's specifications (PrepX RNA-Seq for Illumina Library kit, Takara Bio USA). Libraries were enriched and indexed using 12 cycles of amplification (LongAmp Taq 2x MasterMix, New England BioLabs Inc.) with PCR (polymerase chain reaction) primers which included a 6 bp index sequence to allow for multiplexing (custom oligo order from Integrated DNA Technologies). Excess PCR reagents were removed using magnetic bead-based cleanup (PCR Clean DX beads, Aline Biosciences). RNA integrity was checked with a 2200 TapeStation (Agilent Technologies), and after libraries were created, they were quantified by QPCR (Kapa Biosystems). Libraries were pooled and sequenced on one lane of a HiSeq 2500 high output v3 flow cell using single end, 50 bp reads (Illumina).

2.11.2. RNA-Seq data analysis

RNA-Seq data was analyzed using the RAVED (Reproducible Analysis and Validation of Expression Data) pipeline (https://github.com/HimesGroup/raved) (Kan, 2018). Briefly, quality control (QC) metrics for raw reads were obtained with FastQC (Andrews, 2021) (v.0.11.7). Reads for each sample were aligned with STAR software (Spliced Transcript Alignment to a Reference, v. 2.5.2b) to reference Homo sapiens build 38 UCSC (University of California, Santa Cruz) file (hg38) genome obtained from the Illumina, Inc. iGenomes resource (Dobin et al., 2013). Additional QC parameters were obtained to assess whether reads were appropriately mapped: Bamtools (v.2.3.0) (Barnett et al., 2011) was used to count/summarize the number of mapped reads, including junction spanning reads, and the Picard Tools (v.1.96; http://picard.sourceforge.net) RnaSeqMetrics function was used to compute the number of bases assigned to various classes of RNA, according to the hg38 refFlat file available as a UCSC Genome Table. For each sample, HTSeq (v.0.6.1) was used to quantify genes based on reads that mapped to the provided hg38 reference files (Anders et al., 2015). The DESeq2 R package (v. 1.26.0) was used to measure the significance of differentially expressed genes between the treatment and control samples for the provided 12 treatments and create plots of the results (Love et al., 2014). The reported adjusted p-values are false-discovery rate corrected according to the procedure in DESeq2 that accounts for the large number of comparisons made. An adjusted p-value < 0.05 was considered significant. The Gene Set Enrichment Analysis (GSEA) R package fgsea (v.1.12.0) was used to perform enrichment analysis using gene sets from Reactome and KEGG (Kyoto Encyclopedia of Genes and Genomes) pathway annotations downloaded from Molecular Signatures Database (MSigDB) (v.6.2), and pathways with gene number > 15 and < 500 were included for analysis (GSEA | MSigDB | MSigDB Collections, 2021; Subramanian et al., 2005). P-values for enriched pathways were based on the distribution of enrichment scores following 10,000 permutations, and subsequently, q-values were obtained using the Benjamini-Hochberg approach. Pathways with a q-value < 0.05 were considered significant. Pathways with p-values < 0.005 were collapsed using the collapsedPathways function in fgsea to reduce the number of pathways with highly overlapping sets of genes.

2.12. Statistical analysis

The sanding, incineration, and cellular exposure experiments were all performed in triplicates. The real-time aerosol characteristics (particle number concentrations and aerosol size distributions) were averaged across the triplicate experiments and the resulting aerosol data analysis was performed in the TSI Aerosol Instrument Manager software (AIM, v9.0). In the LDH release and metabolic activity assays, statistical analysis was performed on an average of 6 samples for each exposure condition. ROS assay statistical analysis was performed on an average of 4 samples for each exposure condition. Fold-changes $> 20\%$ were deemed to be statistically significant. The cytokine/chemokine data were presented as the mean $\pm$ standard error of mean (SEM) of 3 samples ($n = 3$) and statistical significance was reported with respect to the negative control (culture media). Statistical analyses for all toxicological data were performed on GraphPad© Prism using one-way ANOVA (analysis of variance) tests and corrected for multiple comparisons (with Dunnett's test).

3. Results

3.1. PCM characterization of NEC nanofillers

The detailed PCM properties of the nanofillers used in the synthesis of the NECs, i.e., iron oxide (Fe_2O_3) and DPP-Red, are summarized in Table S1 and described further in the **SI** text. Briefly, the TEM-measured average primary particle diameters of the utilized nanofillers Fe_2O_3 (small), Fe_2O_3 (large), and DPP-Red were 37 nm, 150 nm, and 43 nm, respectively. Fig. S4A depicts the images of the synthesized NECs after being applied on the quartz plates, showing the characteristic color shades of the different nanofillers.

3.2. Commercial insulation materials: are they nano-enabled building materials?

The photographed images of the INS1 and INS2 insulation blankets are shown in Fig. S4(B–C). Prior to investigating the various lifecycle scenarios and associated occupational health implications of the insulation materials, an important question needed to be addressed as to whether these commercial insulations (INS1, INS2) are indeed nano-enabled materials containing nanoscale particles that are intentionally incorporated into their matrices. Fig. S5 shows the SEM/TEM images of INS1 and INS2 at different magnifications and the corresponding EDX surface elemental surveys of the observed nanoparticles on the material surface. Morphologies of both materials look similar with irregularly shaped flaky fragments with rounded edges lying on the top of or in the empty space between straight, smooth fibrous structures. The fragments span a size range from tens of microns down to the nanoscale size (<100 nm), providing evidence for the presence of nanoscale materials in the insulations (encircled in red in the images). The EDX elemental composition of the nanoparticles shows the presence of elements expected in accordance with the manufacturer provided MSDS (material safety data sheet) compositions **(**Table 1**)** of INS1 and INS2, as well as several other heavy metals not described in the MSDS (Fig. S5**; INS1:** O, Si, C, Al, Mg, Zr, Cr, Fe, Co, Ca, Sn; **INS2:** O, Si, C, Al, Sn, Mg, Ca, Zr, Cr, Fe), indicating the presence of nanoscale metals/metal oxides in the insulation materials. It is not known whether these nanoscale particles were intentionally incorporated during the industrial manufacture of the insulations to impart certain functional properties or they were unintentionally introduced into the insulation fabric during the fibrous silica aerogel synthesis from raw materials containing trace amounts of these heavy metals. Nevertheless, it is clear that the insulations INS1 and INS2 can be classified as NEBMs containing a mixture of nanoscale heavy metals or metal oxide particles.

Furthermore, the ICP-MS analysis (Fig. S6) of the bulk insulation samples confirms the presence of various metals including transition metals in significant concentrations (**INS1:** Si (18.8 wt%), Ca (3.87 wt %), Al (2 wt%), Mg (0.69 wt%), B (0.34 wt%), Na (0.14 wt%), Ti (0.1 wt %), Fe (0.06 wt%), S (0.04 wt%), Sr (0.03 wt%), K (0.02 wt%), Zr (0.01 wt%); **INS2:** Si (16 wt%), Ca (12.5 wt%), Al (5.5 wt%), Fe (1.34 wt%), B (0.91 wt%), Mg (0.54 wt%), K (0.35 wt%), Na (0.22 wt%), Ti (0.16 wt %), S (0.09 wt%), Sr (0.08 wt%), P (0.04 wt%), Ba (0.02 wt%), Zr (0.01 wt%), Mn (0.01 wt%)). The total metal content of the bulk insulation materials is found to be quite high at 26.1 wt% for INS1 and 37.8 wt% for INS2, which points to a possible intentional use of such metallic nanoparticles to enhance the mechanical and thermal properties of the insulations. The mass concentrations of the remaining measured elements for both INS1 and INS2 are summarized in **SI Excel File 1.**

3.3. Sanding of NEBMs: released LCPM characteristics

In this section, the real-time released aerosol characteristics during the mechanical degradation via sanding of insulation materials INS1 and INS2 under predefined operational conditions are summarized as well as the subsequent PCM characterization of the collected sanded dusts to assess whether nanomaterials embedded in the insulations are released into the air during sanding of NEBMs.

3.3.1. Real-time LCPM monitoring

Fig. 1 shows the real-time evolution of the aerosol number concentration in the sanding chamber during the sanding operations on INS1 and INS2 using the OPS (Fig. 1A, aerodynamic sizes 0.3–10 μm) and SMPS (Fig. 1C, mobility sizes 10–300 nm) instrumentation, as well as the real-time OPS aerodynamic size distributions (Fig. 1B, sizes 0.3–10

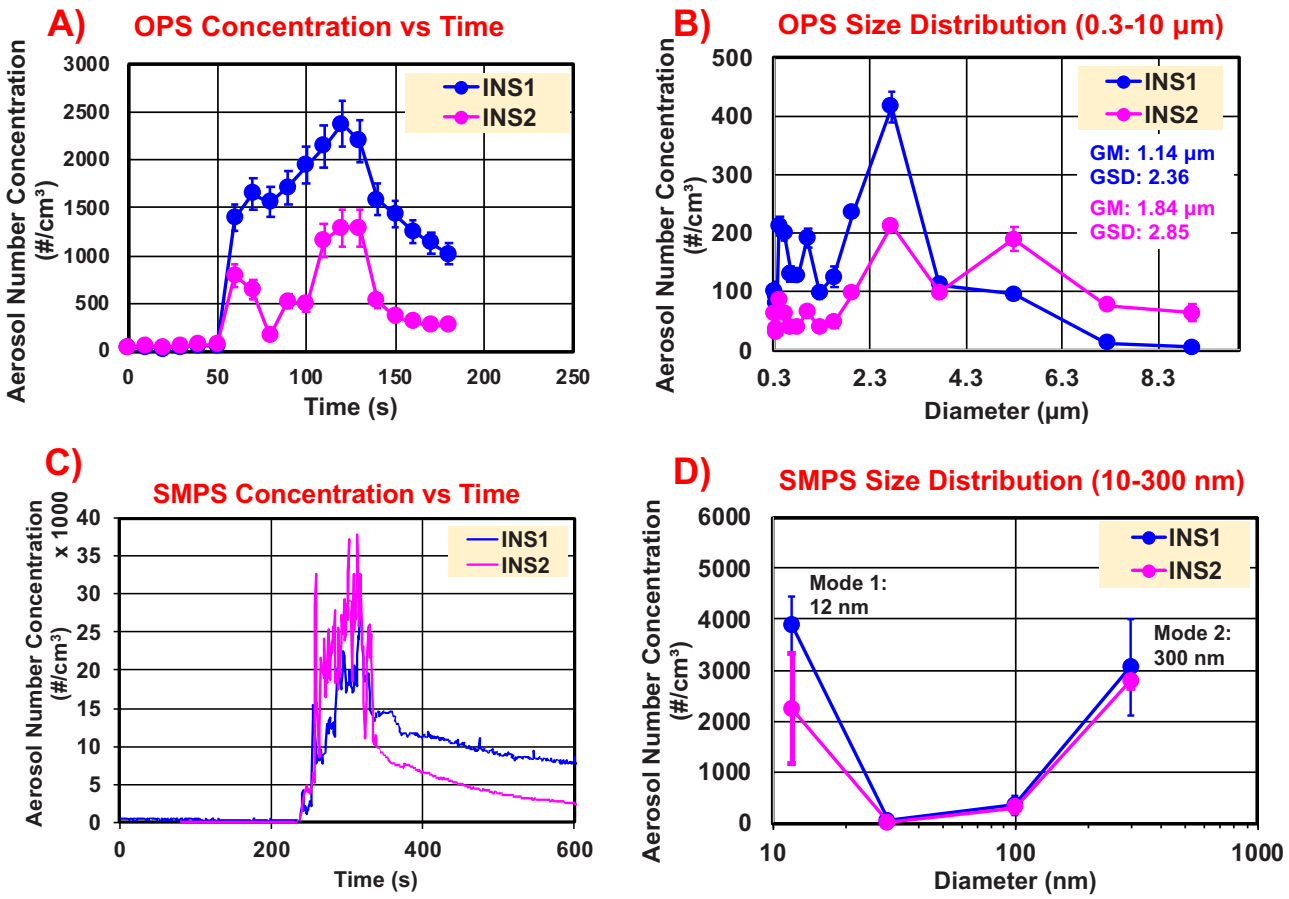

Fig. 1. Real-time released aerosol investigations using TSI OPS (0.3–10 µm) and SMPS (10–300 nm) for the sanding of insulations, INS1 and INS2. A) OPS time trace of particle number concentrations; B) OPS size distributions at the maximum concentration timestamp; C) SMPS time trace of particle number concentrations; and D) SMPS size distributions at the maximum concentration timestamp.

µm) and SMPS mobility size distributions (Fig. 1D, sizes 10–300 nm) of the released LCPM from INS1 and INS2 captured at the timepoints of maximum particle number concentration. It is clear from both real-time instruments that the particle number concentration increases significantly as sanding progresses with respect to the background levels (before sanding) and reaches a peak ~60 s after the start of sanding, which also is the sanding duration employed, and falls off to background levels gradually after the peak when sanding stops. The peak OPS particle number concentration reaches ~2500 particles/cm^3 for INS1 versus ~1500 particles/cm^3 for INS2. On the other hand, the peak SMPS nanoparticle number concentration reaches ~37,000 particles/cm^3 for INS2 versus ~30,000 particles/cm^3 for INS1. Although the peak number concentrations differ slightly between the two insulations, the particle generation curve over time appears to be similar between both materials for the larger particles and the nanoparticles. The OPS number-size distributions of the insulations are slightly different (Fig. 1B), with the geometric mean aerodynamic particle diameter and geometric standard deviation of 1.14 µm (σ_g = 2.4) for INS1 having a single large peak, whereas it is 1.84 µm (σ_g = 2.85) for INS2, which shows a bimodal distribution with two smaller peaks. The SMPS nanoparticle size distribution of released sanding LCPM shows two prominent modes at 12 nm and 300 nm for both insulations (Fig. 1D).

The insulation sanding dusts were also re-aerosolized using the TSI fluidized bed chamber and the resulting aerosol particle number concentration as a function of aerodynamic diameter was measured (Fig. S7). The mean geometric aerodynamic diameter of the larger particles is 1.17 µm (σ_g = 1.88) for INS1 whereas 1.13 µm (σ_g = 1.65) for INS2, showing that the aerosolized sanding dust consists of both micron-sized and submicron-sized particles, consistent with real-time OPS measurements from the sanding chamber.

The gravimetric analysis of the time-integrated and size-fractionated sanded PM shows nearly 63–67% by weight of particles in the $PM_{2.5}$ size fraction whereas the remaining mass fraction (33–37 wt%) belongs to particles larger than 2.5 µm aerodynamic size (data not shown), indicating that majority of the sanded LCPM of the insulations by mass lies in the inhalable size fraction.

3.3.2. *Morphology and elemental composition of released LCPM*

Fig. 2 shows the SEM/TEM images at different magnifications along with the EDX elemental information on the total sanded dust collected from INS1 (Fig. 2A-B) and INS2 (Fig. 2C-D). The corresponding EDX spectra on the insulation dusts are shown in Fig. S8**.** The micrographs show the presence of several micron-sized random-shaped fragments along with a few submicron aggregates for both materials in the SEM images, as well as nanoscale (<100 nm) structures in the TEM images. Elemental mapping of the submicron aggregates reveals the presence of the characteristic elements (including transition metals) of the pristine insulation materials (as indicated in the MSDS and PCM characterization of the insulations described in the previous section) in the released LCPM, suggesting the presence of released nano-metals in the sanded dusts. The major elemental species observed for the INS1 sanded dust are O and Si, whereas the minor species are Mg and Al. For the INS2 sanded dust, the major elements observed are O, Si, Al, and Mg, and the minor ones are S, Cl, P, Ca, and Fe.

The bulk elemental compositions of the collected sanded dust of INS1 and INS2 were also measured using ICP-MS (Fig. 2E-F). A high mass fraction of total metal content is observed for both dusts, with INS1 sanded dust containing 15.3 wt% total metals, whereas for INS2 sanded

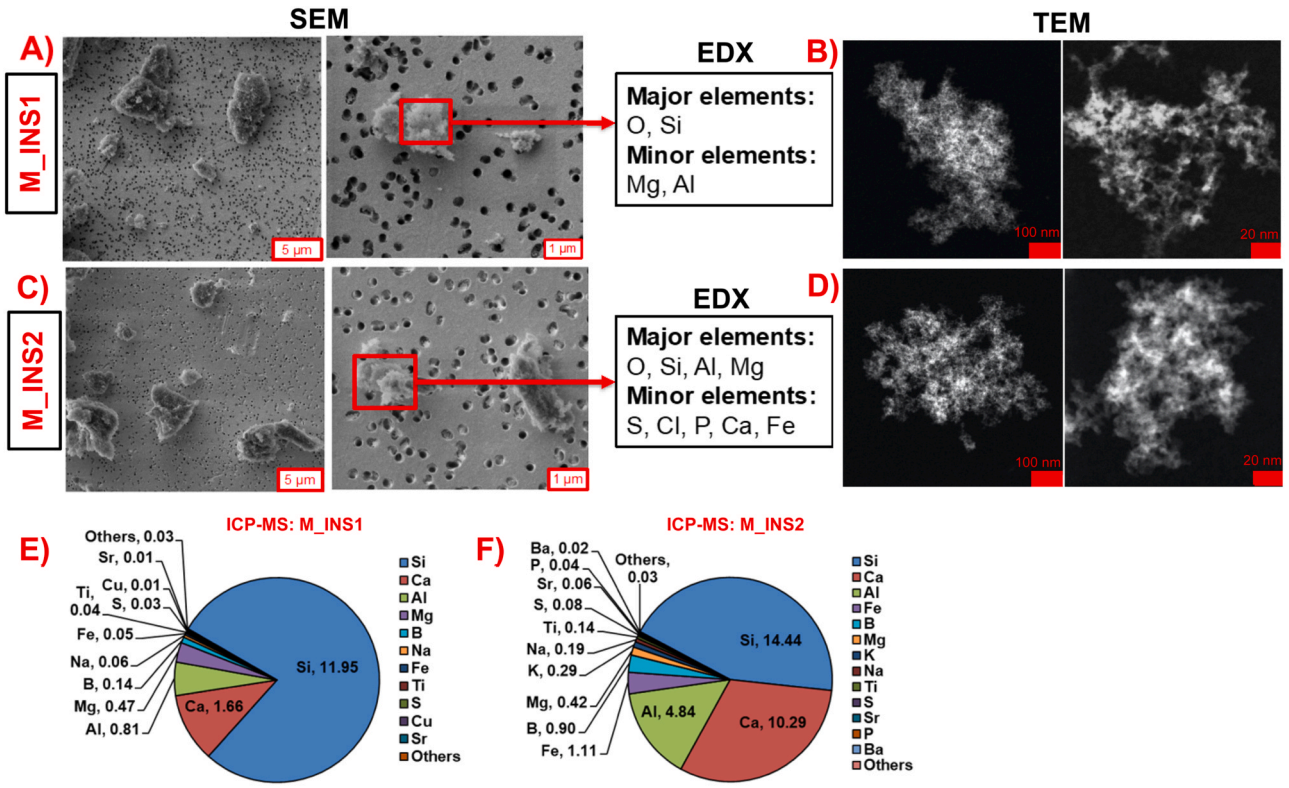

Fig. 2. Released sanding dust physicochemical and morphological characterization for insulations INS1 and INS2. SEM/EDX and TEM on sanding dust from A, B) INS1and C, D) INS2. ICP-MS bulk elemental composition on the sanding dust of E) INS1 and F) INS2.

dust it is much higher at 32.9 wt%. The quantitative mass percentages of the various prominent elements measured in the sanded dust from INS1 are Si (11.95 wt%), Ca (1.66 wt%), Al (0.81 wt%), Mg (0.47 wt%), B (0.14 wt%), Na (0.06 wt%), Fe (0.05 wt%), Ti (0.04 wt%), S (0.03 wt %), Cu (0.01 wt%), and Sr (0.01 wt%), whereas those from INS2 are Si (14.44 wt%), Ca (10.29 wt%), Al (4.84 wt%), Fe (1.11 wt%), B (0.90 wt %), Mg (0.42 wt%), K (0.29 wt%), Na (0.19 wt%), Ti (0.14 wt%), S (0.08 wt%), Sr (0.06 wt%), P (0.04 wt%) and Ba (0.02 wt%). Mass concentrations of the remaining metals in both sanded dusts are tabulated in **SI Excel File 1.**

3.4. Incineration of NEBMs: released LCPM characteristics

In this section, we present the real-time released aerosol characteristics, PCM properties of released LCPM, time-integrated and size-fractionated collected LCPM data, and residual ash yields from the

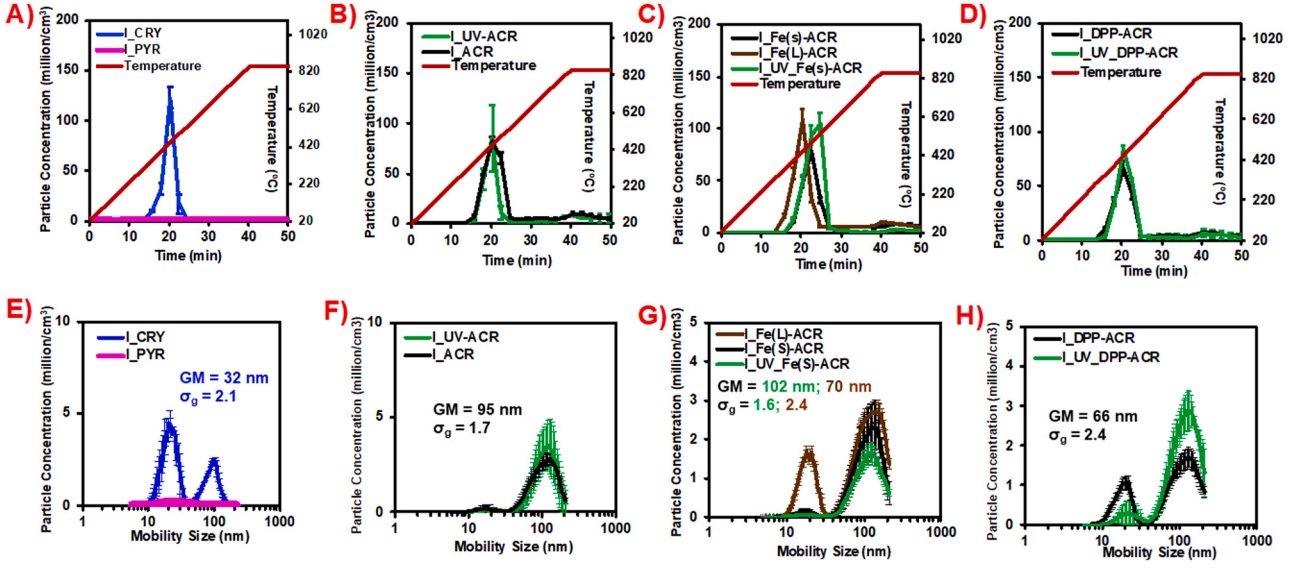

Fig. 3. Real-time released aerosol investigations using TSI SMPS 3080 during incineration of insulations and coatings (w, w/o UV-aging). (A, E) PNC over time, mobility size distribution of INS1, INS2; (B, F) PNC over time, mobility size distribution of ACR, UV_ACR; (C, G) PNC over time, mobility size distribution of Fe(s) _ACR, UV_Fe(s)_ACR, Fe(L)_ACR; **(D, H)** PNC over time, mobility size distribution of DPP_ACR and UV_DPP-ACR. PNC: particle number concentration; GM: geometric mean mobility diameter; σ_g: geometric standard deviation.

incineration of the insulation materials and the NECs (unaged and UV-aged), under the predefined thermal decomposition conditions, to identify factors affecting nano-release dynamics and LCPM PCM properties during the incineration of NEBMs. In more detail:

3.4.1. Incineration of insulation materials

3.4.1.1. Real-time LCPM monitoring. Fig. 3A shows the real-time evolution of SMPS-measured nanoparticles (mobility size: 5–250 nm) number concentration with respect to time during the incineration of the insulation materials INS1 and INS2. Correspondingly, Fig. 3F presents the SMPS-measured nanoparticle size distributions (snapshots at the timepoint of maximum particle number concentration) during incineration of the insulations. During the incineration, the temperature increases linearly with time starting from the room temperature at the predefined heating rate of 20 °C/min up to a maximum of 850 °C until ~40 min and staying constant for 10 min before the furnace begins to cool off. For the insulation materials, only the INS1 appears to undergo thermal degradation with the aerosol generation beginning around 15 min (~400 °C) and the peak emitted particle number concentration reaching ~150 million particles/cm^3 around 20 min (~450 °C), followed by a rapid decrease in particle concentration. Comparatively, the insulation INS2 does not generate significantly more particles than the baseline, suggesting a lack of thermal degradation of the material even at the high final temperature of 850 °C, although mass loss of the insulation was observed and was accompanied by release of several decomposition gaseous byproducts and volatile organic compounds (described in subsequent sections). The INS1-emitted incineration PM exhibits a bimodal nanoparticle size distribution with peaks at 22 nm and 102 nm, with an overall geometric mean mobility diameter of 32 nm ($\sigma_g = 2.1$).

Real-time PM monitoring using the APS for the larger particles (aerodynamic size: 0.5–20 μm) was also performed for the incinerated insulations, however, the peak number concentrations observed are nearly four orders of magnitude lower than the SMPS-measured nanoparticle concentrations (~15,000–25,000 particles/cm^3) with the observed geometric mean aerodynamic size between 1.2 and 1.5 μm (data not presented). No significant emitted particles compared to the baseline are detected in the APS during the incineration of the INS2 insulation, similar to the SMPS measurements, confirming that the INS2 insulation did not disintegrate thermally.

3.4.1.2. Elemental composition of released $PM_{2.5}$. The released and collected $PM_{2.5}$ from the incineration of the insulations were analyzed for their bulk elemental composition using ICP-MS to determine the potential release of the nanoscale metal/metal oxides in the pristine insulations into the airborne PM. Fig. 4**A-B** shows the quantitative mass percentage concentrations of the ICP-MS-determined metals in the incineration $PM_{2.5}$ from the insulations (INS1, INS2).

The total metal concentration measured in I_INS2 is 8.4 wt%,

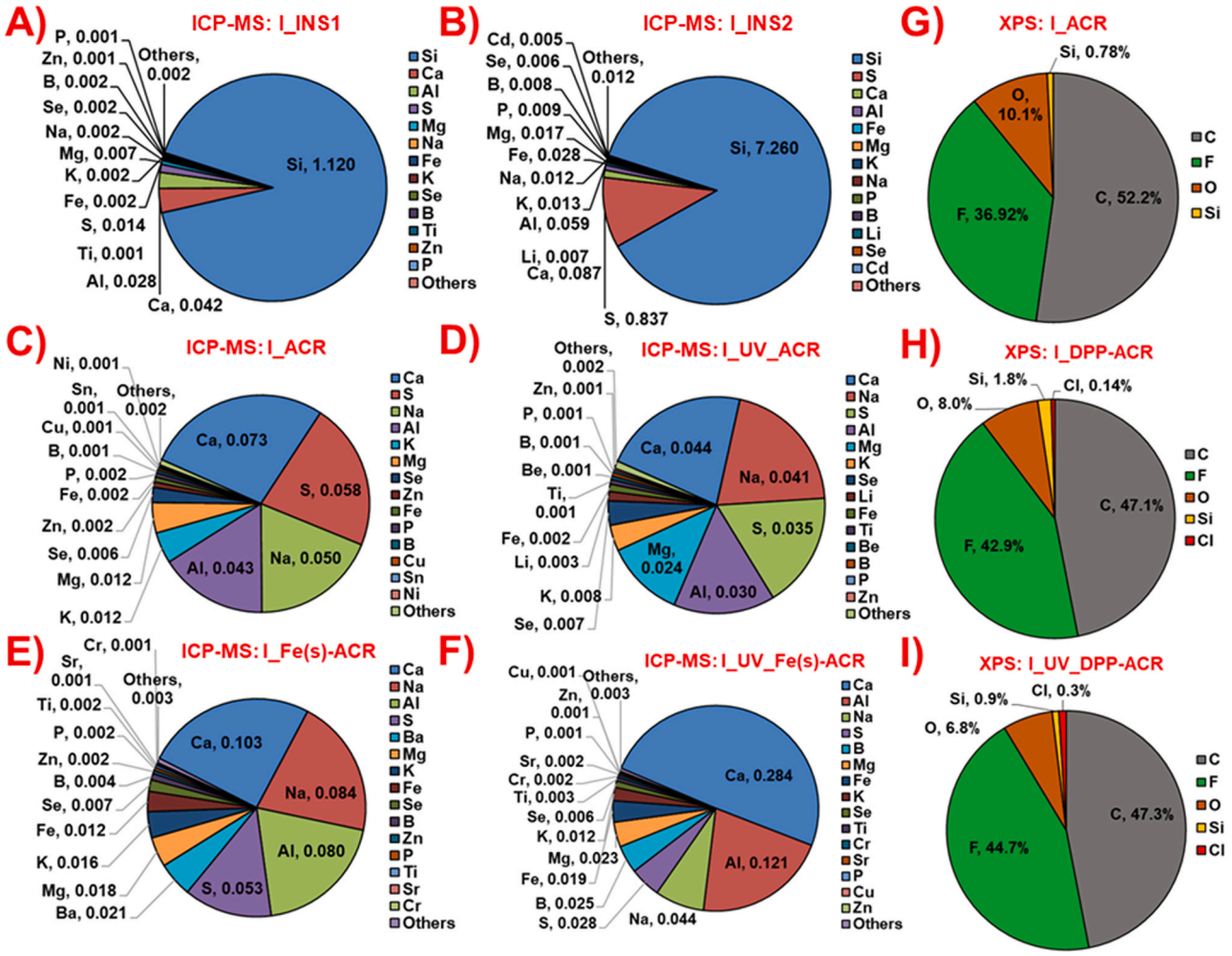

Fig. 4. Released $LCPM_{2.5}$ bulk elemental composition for incineration of insulations A) INS1 and B) INS2 using ICP-MS; incineration of coatings C) ACR, D) UV_ACR, E) Fe(s)-ACR and F) UV_Fe(s)-ACR using ICP-MS; and $LCPM_{2.5}$ surface elemental composition for incineration of coatings G) ACR, H) DPP-ACR and I) UV_DPP-ACR using XPS.

significantly higher than in I_INS1 (1.2 wt%), mostly dominated by the high concentration of Si in I_INS2 (7.3 wt%) compared to I_INS1 (1.1 wt %). Both I_INS1 and I_INS2 are found to contain several other metals in trace-level concentrations (<0.1 wt%), including but not limited to Ca, Al, Mg, Na, Fe, K, Se, Ti, Zn, and Cd (Fig. 4**A-B, SI Excel File 1**), providing evidence of release of the inherent metallic nanoparticles in the insulations into the incineration aerosol PM.

3.4.1.3. Evolved gas chemical analysis. Figs. S9–12 summarize the chemical spectral information obtained from FTIR (absorbance vs. wavenumber) and GC-MS (intensity vs. retention time) on the evolved off-gases during the thermal decomposition of INS1 (snapshot around 523 °C) and INS2 (snapshot around 612 °C), respectively in the TGA. The spectra identify a mixture of aliphatic (including alicyclic) and aromatic compounds, with alcohol, aldehyde, and ketone functional groups in the gaseous off-stream. Common gaseous species identified for both insulations included significant traces of cyclohexene, 4-hexen-1-ol, and benzaldehyde, and a large mixed peak corresponding to unidentified halogenated compound(s). Additionally, for INS1, α-methylstyrene (a monomer for the poly(α-methylstyrene) (PAMS) synthetic polymer) is identified, thus pointing to the presence of this hydrophobic polymer in INS1 (Madras et al., 1996). In contrast, for INS2, additional volatile organics namely, formaldehyde, hexamethylcyclotrisiloxane, and cis-cyclooctene are identified. The presence of hexamethylcyclotrisiloxane as a decomposition byproduct indicates the presence of organosilicon polymers such as polydimethylsiloxane in the INS2 matrix (Clausen et al., 2019). Furthermore, the presence of the cyclic olefin (cis-cyclooctene) fragment suggests the presence of corresponding polyoctenamers as the hydrophobic additive in the INS2 matrix (Martinez et al., 2014).

3.4.2. Incineration of NECs

3.4.2.1. Real-time LCPM monitoring. Fig. 3B-D shows the real-time evolution of SMPS-measured nanoparticles (mobility size: 5–250 nm) number concentration with respect to time during the incineration of the unaged/UV-aged NECs. Correspondingly, Fig. 3**(F-H)** presents the SMPS-measured nanoparticle size distributions (snapshots at the time-point of maximum particle number concentration) during incineration of the NECs. Incineration of the NECs (both unaged and UV-aged) shows similar particle generation profiles with time, with nanoparticle number concentrations reaching their maximum at ~20–22 min (~450–490 °C) after the start of incineration. No significant differences are observed in the peak nanoparticle number concentrations between the unaged NECs and the corresponding UV-aged NECs, for either the ACR, Fe(s)-ACR, or DPP-ACR coatings. However, the Fe_2O_3 nanofiller containing coatings (Fe(s)-ACR, Fe(L)-ACR, UV_Fe(s)-ACR) show a slightly higher peak particle number concentration at ~100 million particles/cm^3 compared to the ACR/UV_ACR and DPP-ACR/UV_DPP-ACR coatings, which show maximum nanoparticle emission at ~75 million particles/cm^3. Similarly, the SMPS mobility size distributions of the released aerosol are similar between the unaged and UV-aged NECs and were bimodal in all cases. The observed geometric mean mobility diameters for the incineration LCPM from coatings are 95 nm (σ_g = 1.7), 102 nm (σ_g = 1.6), and 66 nm (σ_g = 2.4), for ACR/UV_ACR, Fe(s)-ACR/UV_ Fe(s)-ACR, and DPP-ACR/UV_DPP-ACR coatings, respectively. The incineration LCPM from the unaged coating with the larger size of Fe_2O_3 nanofiller (Fe(L)-ACR) shows a significantly different geometric mean diameter at 70 nm (σ_g = 2.4) compared to the NEC with the smaller Fe_2O_3 nanofiller (geometric mean = 102 nm, σ_g = 1.6).

The APS-measured real-time aerosol number concentrations and aerodynamic size distributions for the NECs were quite similar to the insulations, with nearly four orders of magnitude lower particle number concentration (~10^4 particles/cm^3) than the SMPS-measured nanoparticles and mean aerodynamic particle sizes close to 1 μm (data not presented).

3.4.2.2. Elemental composition of released $PM_{2.5}$. The released and collected $PM_{2.5}$ from the incineration of the unaged/UV-aged NECs were also analyzed for their bulk elemental composition using ICP-MS to determine the potential release of the nanoscale metal/metal oxides in the pristine NECs into the airborne PM. Fig. 4**C-F** shows the quantitative mass percentage concentrations of the ICP-MS-determined metals in the incineration $PM_{2.5}$ from the NECs (except for the DPP-Red containing coatings for which XPS was performed on the $PM_{2.5}$).

Interestingly, the total metal concentrations measured in the incineration $PM_{2.5}$ from coatings are significantly lower than those observed for the insulation materials (Fig. 4C-F**, SI Excel File 1**). The observed weight concentrations of the total metals in incineration LCPM from unaged and UV-aged coatings are I_ACR (0.27 wt%), I_UV_ACR (0.2 wt %), I_Fe(s)-ACR (0.41 wt%), I_UV_Fe(s)-ACR (0.57 wt%), and I_Fe(L)-ACR (0.24 wt%). Prominent elements detected in the released $PM_{2.5}$ include but are not limited to Ca, Al, Mg, Na, S, B, K, Fe, and Ti. One of the critical questions to be addressed is whether the metal oxide nanofiller (Fe_2O_3) in the acrylic coating matrix is released into the aerosol during incineration. Examining the concentration of Fe metal in the incineration LCPM from the Fe_2O_3-containing coatings, the mass concentration of Fe is I_Fe(s)-ACR (0.012 wt%), I_UV_Fe(s)-ACR (0.019 wt %), and I_Fe(L)-ACR (0.005 wt%), which is ~2–9 times higher than for the control acrylic matrix-only coatings, I_ACR (0.002 wt%) and I_UV_ACR (0.002 wt%), indicating probable release of the Fe_2O_3 nanofiller in $PM_{2.5}$, although the exact physicochemical and morphological state of the released Fe is not investigated here.

In addition, to assess the possible release of the organic nanofiller (DPP-Red) from the incineration of DPP-ACR/UV_DPP-ACR, XPS analysis on the released $PM_{2.5}$ was performed to detect the presence of the signature element (chlorine, Cl) that is part of the molecular structure of DPP-Red ($C_{18}H_{10}Cl_2N_2O_2$) organic nanofiller. Fig. 4**G-I** shows the surface elemental atomic composition of the incineration $PM_{2.5}$ from the ACR, DPP-ACR, and UV_DPP-ACR coatings. The high elemental concentrations of carbon (C: ~47–52 at%) and oxygen (O: ~7–10 at%) reflect the presence of a substantial concentration of carbonaceous and organic compounds in the released particles from the incineration of coatings. Importantly, I_DPP-ACR and I_UV_DPP-ACR show the presence of a tiny atomic percentage of Cl in the PM at 0.14% and 0.3% respectively, while no Cl is observed for I_ACR, indicating that DPP-Red could be partly released in the aerosol during incineration, although most of it could have been oxidized and its physicochemical composition might have significantly transformed at the high incineration temperatures involved.

3.4.3. Incineration LCPM mass-size distributions and PM/residual ash yields

The mass-aerodynamic size distributions of the size-fractionated and collected PM in the Harvard CCI during the incineration of the insulations and NECs for two size fractions, $PM_{2.5}$ and $PM_{>2.5}$ were analyzed (data not shown). Consistent with data from previous studies (Singh et al., 2019a), a majority of the PM mass (80–87 wt%) is contained in the aerodynamic size fraction below 2.5 μm ($PM_{2.5}$), indicating that most of the released particles by weight during incineration are fine, inhalable particles. A minuscule amount of incineration PM is collected from INS2, as is expected from its real-time APS and SMPS aerosol measurements, that did not show significantly more released particle number concentration compared to the baseline.

The mass percentage yields of the generated and collected $PM_{2.5}$ and the remaining residual ash after incineration with respect to the starting quantity of the pristine insulations/coatings are summarized in Table S2. It can be observed that the NECs yield a higher quantity of the released $PM_{2.5}$ (~5–7 wt% of starting material) than the insulation INS1 (~0.61 wt%), whereas INS2 has a negligible $PM_{2.5}$ yield (~0.02 wt%).

Conversely, as expected from mass balance, the insulations leave behind a much higher percentage of the residual ash (~89 wt% for INS1; ~99 wt% for INS2) than the coatings (~42–45 wt%).

The instantaneous TGA data on the mass loss of insulations as a function of temperature ramp-up are plotted in Fig. S13 for INS1 and Fig. S14 for INS2. Consistent with the gravimetric analysis on the residual ash collected in the INEXS platform, the TGA data also indicate a higher total mass loss of the insulation INS1 (10.2 wt%) compared to INS2 (5.3 wt%) over the entire temperature regime up to 800 °C, thus yielding corresponding residual ash amounts of 89.8 wt% and 94.7 wt% respectively of the starting insulation weights.

3.5. Colloidal characterization of $LCPM_{2.5}$ particles

Table S3 summarizes the detailed colloidal properties of the collected $PM_{2.5}$ particles from the sanding and incineration of the insulations and coatings, that were dispersed in deionized water at their critical sonication energy at $t = 0$ and then diluted in culture media (EMEM + 10% FBS) at $t = 0$ and $t = 24$ h (to indicate the colloidal stability of the dispersed particles in cellular media over 24 h). The LCPM dispersions in the culture medium appear to be mostly stable with minimal changes over 24 h in the zeta-average intensity-weighted hydrodynamic diameter (d_H, nm), the polydispersity index (PdI), and the zeta potential (ζ, mV) of the particles. In more detail:

3.5.1. Colloidal characteristics of insulation LCPM

For the insulation materials, it can be observed that the sanded LCPM displays a higher average d_H and a moderately more negative ζ than the incineration LCPM, although all LCPM suspensions are polydisperse. For example, in the culture medium at 24 h, M_INS1 and M_INS2 display an average d_H of 436 nm (PdI = 0.3) and 418 nm (PdI = 0.5) respectively and an average ζ around − 10 mV, whereas I_INS1 has a much lower d_H at 85 nm (PdI = 0.2) and a ζ around − 8 mV. Since a negligible amount of incinerated $PM_{2.5}$ particles were released and therefore collected from INS2, there was no colloidal characterization performed for these particles.

3.5.2. Colloidal characteristics of NEC LCPM

The incinerated LCPM from NECs displays different hydrodynamic sizes depending on the nanofiller type and prior UV-aging of the NEC. For example, I_ACR, I_Fe(s)-ACR, and I_DPP-ACR show average hydrodynamic diameters in culture medium (at 24 h) of 100.6 nm, 55.1 nm, and 20.6 nm respectively, indicating the effect of the nanofiller type on the LCPM colloidal size. In addition, the hydrodynamic diameter of I_Fe (L)-ACR (with larger Fe_2O_3 nanofiller size) is 142.5 nm, which is higher than that of I_Fe(s)-ACR at 55.1 nm. The hydrodynamic diameters of the incinerated LCPM from the corresponding UV-aged NECs are different from the unaged NECs. The I_UV_ACR, I_UV_Fe(s)-ACR, and I_UV_DPP-ACR have hydrodynamic diameters of 19 nm, 78 nm, and 70 nm, respectively. The zeta potentials of the NEC LCPM in culture media stay in a narrow range between − 13 mV and − 8 mV. The PdI of the NEC LCPM in media ranged from 0.2 to 0.7 indicating that the particle suspensions are polydisperse.

In comparison, the comparator MS-WF particles have the largest hydrodynamic size at 1002 nm, PdI of 0.2, and a zeta potential of − 11 mV in culture medium after 24 h.

3.6. In vitro toxicity assessment of $LCPM_{2.5}$ particles

Here we describe the results of the cytotoxicity assessment of the $LCPM_{2.5}$ obtained from the sanding and incineration of the insulations and coatings on the Calu-3 human lung cell line, using the assays for the endpoints of cellular viability (LDH release), metabolic activity and oxidative stress at the two administered LCPM doses of 20 and 75 μg/mL. In more detail:

3.6.1. Cytotoxicity of insulation LCPM

Fig. 5 (A, B, C) shows the results for the LDH release, metabolic activity, and ROS production in the exposed cells for the sanding and incineration LCPM of the insulation materials, namely, M_INS1, M_INS2, and I_INS1, at the two doses. As described earlier, collected incineration $LCPM_{2.5}$ from INS2 was negligible and therefore not included in the cytotoxicity investigations. Neither of the LCPM samples induced significant LDH release or changes in metabolic activity after 24 h or increase in ROS production after 6 h in the treated cells at either dose, compared to the negative control and the vehicle control, indicating that the released PM from the sanding or incineration of these insulation materials is not cytotoxic, at the investigated doses. Furthermore, the comparator material, i.e., MS-WF does not exhibit any cytotoxic response at the studied doses as well.

3.6.2. Cytotoxicity of NEC LCPM

Fig. 5 (D, E, F) shows the cytotoxicity assay results for the incineration $PM_{2.5}$ from both the unaged and the prior UV-aged NECs. None of the incineration LCPM induces significant LDH release at 24 h compared to the negative or vehicle controls at both doses, indicating no effect on the cellular viability of the lung epithelial cells. However, statistically significant increases in metabolic activity of the exposed cells compared to the untreated cells after 24 h is observed at the lower administered LCPM dose (20 μg/mL) for I_ACR (+31%, $p < 0.05$) and at the higher administered LCPM dose of 75 μg/mL for I_ACR (+47%, $p < 0.05$), I_Fe (s)-ACR (+38%, $p < 0.05$), and I_Fe(L)-ACR (+41%, $p < 0.05$), indicating a dose-dependent effect on the metabolic activity of the exposed lung epithelial cells. However, the corresponding incineration LCPM from UV-aged ACR, Fe(s)-ACR, and Fe(L)-ACR did not exhibit any effect on cellular metabolic activity. In addition, increased cellular metabolic activity at the higher dose is observed for I_UV_DPP-ACR (+29%, $p < 0.05$), but not for I_DPP-ACR, suggesting the modulating effect of prior UV-aging on the subsequent incinerated PM bioactivity in the case of DPP-Red nanofiller. The incineration LCPM from unaged/aged NECs does not increase oxidative stress after 6 h in the exposed cells compared to the negative or vehicle controls, however, a small dose-dependent but statistically significant increase in ROS production was observed for I_Fe (L)-ACR at 75 μg/mL compared to 20 μg/mL ($p < 0.05$).

3.7. In vitro inflammatory response assessment of $LCPM_{2.5}$ particles

The supernatants of the exposed lung epithelial cells at the higher LCPM administered dose of 75 μg/mL after 24 h were also analyzed for a diverse panel of inflammatory cytokines and chemokines to assess the in vitro acute inflammatory response to the various LCPM exposures.

3.7.1. Inflammatory response to insulation LCPM

3.7.1.1. Sanding LCPM from insulations. Fig. 6 (A-J) shows the concentrations of selected biomarkers measured in the cellular supernatants from exposures to the sanding LCPM from INS1 and INS2, in addition to the negative and vehicle controls and the comparator material MS-WF. Exposure to M_INS1 results in the significant upregulation or downregulation of several inflammatory biomarkers, compared to the negative control. Biomarkers that are significantly enhanced are TGFα ($p < 0.01$), GM-CSF ($p < 0.01$), IL-6 ($p < 0.05$) (Fig. 6C-E), and MCP-1 ($p < 0.0001$) (Fig. S15F) whereas those that are significantly suppressed are VEGF-A ($p < 0.05$), PDGF-AA ($p < 0.05$), FGF-2 ($p < 0.01$), PDGF-AB/BB ($p < 0.01$), IP-10 ($p < 0.0001$), MDC ($p < 0.0001$), RANTES ($p < 0.05$) (Fig. 6A, B, F-J), IL-4 ($p < 0.01$), and GROα ($p < 0.05$) (Fig. S15D, E). In contrast, exposure to M_INS2 increases the secretion of only one biomarker, i.e., MCP-1 ($p < 0.05$) (Fig. S15F), and significantly suppresses the release of two biomarkers, namely, IP-10 ($p < 0.0001$) and MDC ($p < 0.001$) (Fig. 6H, I). The comparator MS-WF exposure significantly enhances the release of TGFα ($p < 0.01$)

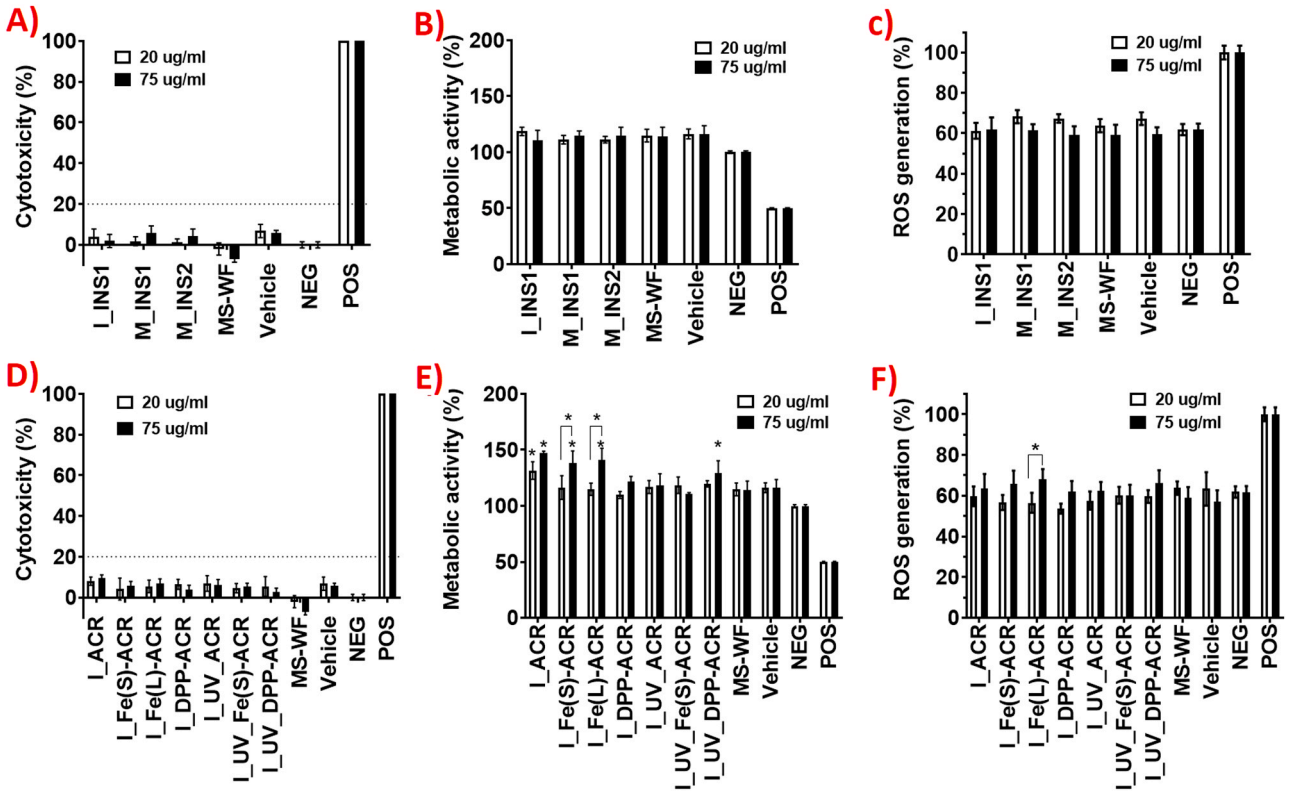

Fig. 5. Acute in vitro cytotoxicity assessment of insulation (top row) and coating (bottom row) $LCPM_{2.5}$ during various lifecycle scenarios in human lung epithelial cells (Calu-3) at 2 doses of 20 and 75 μg/mL: **(A, D)** LDH release at 24 h; **(B, E)** metabolic activity at 24 h; **(C, F)** ROS at 6 h. Statistical analysis was performed on an average of 6 samples (LDH and metabolic activity) and 4 samples (ROS) for each condition; fold-changes > 20% were deemed to be statistically significant.

(Fig. 6 C) and IL-18 ($p < 0.001$) (Fig. S15A), while significantly suppressing IP-10 ($p < 0.0001$), MDC ($p < 0.001$), and RANTES ($p < 0.01$) (Fig. 6H-J).

3.7.1.2. Incineration LCPM from insulations. Incineration LCPM from the insulation INS1 significantly upregulates several biomarkers including PDGF-AA ($p < 0.01$), TGF-α ($p < 0.0001$), GM-CSF ($p < 0.01$), IL-6 ($p < 0.01$) (Fig. 6B-E), IL-1α ($p < 0.05$), and IFNγ ($p < 0.01$) (Fig. S15B-C), while strongly suppressing only the biomarker IP-10 ($p < 0.0001$) (Fig. 6H). The inflammatory response assessment was not able to be performed for the incineration LCPM of insulation INS2 due to its lack of thermal decomposition and therefore no collection of released LCPM, as also mentioned earlier.

3.7.2. Inflammatory response to NEC LCPM

Fig. 6 (K-T) shows the biomarker levels as a result of exposures to the incineration LCPM from the NECs (both unaged and UV-aged prior to incineration), along with the employed controls. Compared to the negative control, I_ACR significantly promotes the release of VEGF-A ($p < 0.01$), PDGF-AA ($p < 0.0001$), TGF-α ($p < 0.0001$), GM-CSF ($p < 0.01$), IL-6 ($p < 0.01$), and TNFβ ($p < 0.01$) (Fig. 6K-O, Q), whereas the corresponding LCPM from I_UV_ACR does not increase the release of any cytokine. However, both I_ACR and I_UV_ACR strongly suppress the secretion of IP-10 ($p < 0.0001$ for both), MDC ($p < 0.0001$, $p < 0.01$, respectively), and RANTES ($p < 0.001$, $p < 0.01$, respectively) (Fig. 6R-T), while only the I_ACR suppresses GROα ($p < 0.001$) and MCP-1 ($p < 0.01$) (Fig. S15K, L). The incineration LCPM from the Fe_2O_3 nanofiller containing acrylic coatings shows consistent upregulation/downregulation of biomarkers between the two Fe_2O_3 nanofiller sizes. Similar to I_ACR, both I_Fe(s)-ACR and I_Fe(L)-ACR display a strong enhancement of the biomarkers VEGF-A ($p < 0.0001$, $p < 0.001$, respectively), PDGF-AA ($p < 0.0001$), TGFα ($p < 0.0001$), GM-CSF ($p < 0.01$, $p < 0.0001$, respectively), and TNF-β ($p < 0.001$) (Fig. 6K-N, Q). Additionally, unlike I_ACR, both I_Fe(s)-ACR and I_Fe(L)-ACR significantly upregulate TNF-α ($p < 0.05$) (Fig. 6 P), whereas I_Fe(s)-ACR alone promotes IL-4 secretion ($p < 0.05$) (Fig. S15J). Both I_Fe(s)-ACR and I_Fe(L)-ACR induce a strong suppression of IP-10 ($p < 0.0001$), MDC ($p < 0.0001$, $p < 0.001$ respectively), RANTES ($p < 0.0001$), (Fig. 6R-T), GROα ($p < 0.05$, $p < 0.01$ respectively), and MCP-1 ($p < 0.05$ for both) (Fig. S15K, L), similar to I_ACR. However, the incineration LCPM from the UV-aged Fe(s)-ACR coating does not enhance the secretion of any inflammatory biomarkers but decreases the release of only two biomarkers, IP-10 ($p < 0.0001$) and RANTES ($p < 0.01$) (Fig. 6R, T). Similar to I_ACR, I_Fe(s)-ACR and I_Fe(L)-ACR, the incineration LCPM from both unaged and UV-aged DPP-Red containing coatings, I_DPP-ACR and I_UV_DPP-ACR, significantly upregulate the biomarkers PDGF-AA ($p < 0.05$, $p < 0.01$, respectively), TGF-α ($p < 0.01$, $p < 0.05$, respectively), and IL-6 ($p < 0.001$, $p < 0.01$, respectively) (Fig. 6L, M, O). Additionally, I_DPP-ACR, but not I_UV_DPP-ACR, stimulates the release of GM-CSF ($p < 0.001$) and TNF-α ($p < 0.01$) (Fig. 6N, P). In contrast, I_UV_DPP-ACR, but not I_DPP-ACR, enhances the release of TNF-β ($p < 0.05$) (Fig. 6Q). Furthermore, unlike I_ACR, I_Fe(s)-ACR and I_Fe(L)-ACR, I_DPP-ACR significantly promotes the secretion of additional cytokines, namely, IL-18 ($p < 0.01$), IL-1α ($p < 0.001$), and IFNγ ($p < 0.05$) (Fig. S15G-I). Both I_DPP-ACR and I_UV_DPP-ACR suppress the release of IP-10 ($p < 0.01$) and MDC ($p < 0.01$), while RANTES is inhibited only in cells treated with I_UV_DPP-ACR ($p < 0.01$) (Fig. 6R-T).

As for the remaining cytokine and chemokine levels, they either did not reach detectable levels in the supernatant (sCD40L, G-CSF, IFNα2, IL-2, IL-3, IL-7, IL-9, IL-12 (p70), IL-17A, IL-17E, IL-17F, MIP-1α, MIP-1β) or did not markedly differ between the various LCPM exposure groups (EGF, Eotaxin, Flt-3 ligand, IL-1β, IL-1ra, IL-5, IL-8, IL-10, IL-13, IL-15, IL-22, IL-27, MCP-3, M-CSF, MIG) (data not shown).

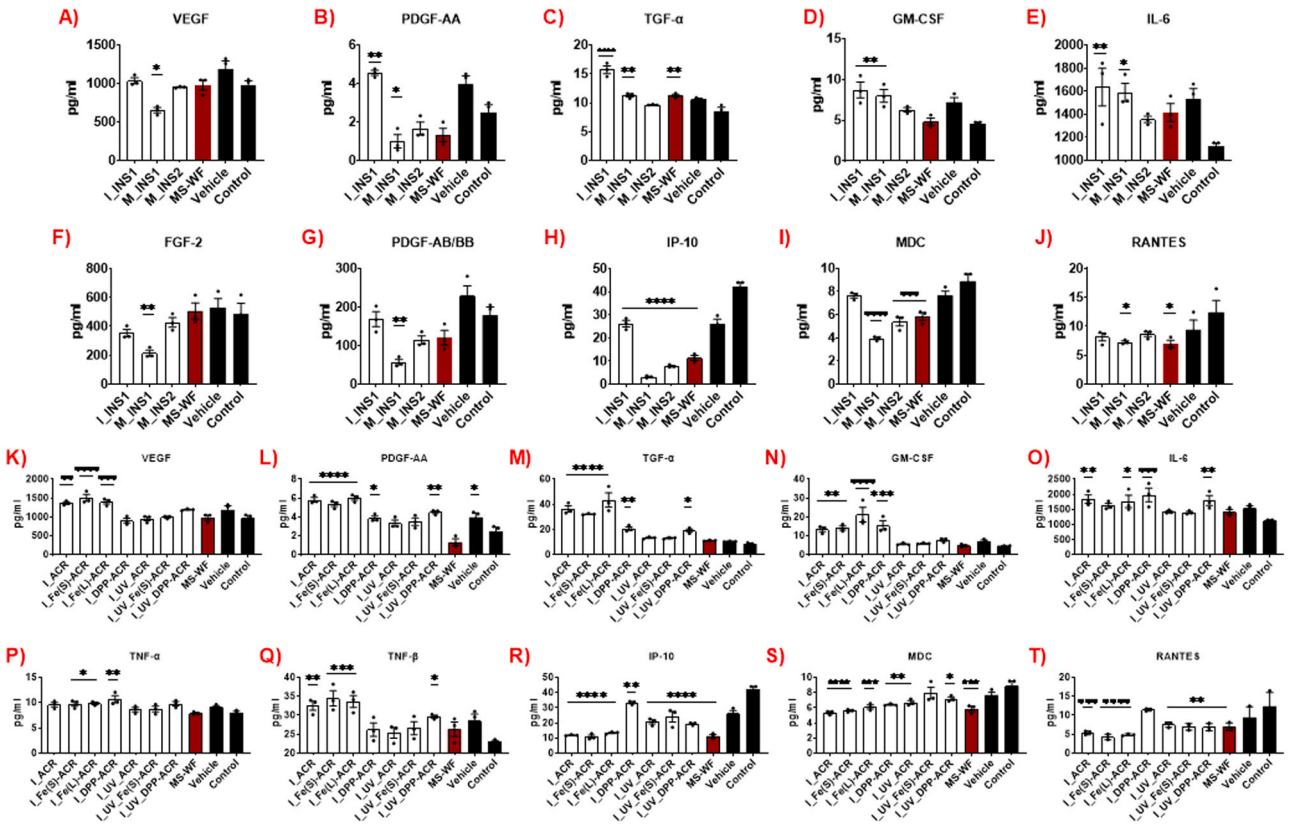

Fig. 6. Acute 24-h inflammatory cytokine and chemokine assessment of coating (A-J) and insulation (K-T) $LCPM_{2.5}$-exposed lung epithelial cells at the higher administered dose of 75 μg/mL (only selected biomarkers shown out of the 48). Data are the mean ± SEM of 3 samples (n = 3). *p < 0.05, **p < 0.01, ***p < 0.001, ****p < 0.0001, versus negative control.

3.8. RNA-Seq transcriptomic profiling of $LCPM_{2.5}$-exposed Calu-3 lung epithelial cells

Differential expression results for genes with adjusted $p < 0.05$ and magnitude Log_2Fold change > 1 for comparisons involving each $LCPM_{2.5}$ material versus the negative control samples are listed in the **SI Excel File 2.** Fig. 7 shows the heatmap of a selected subset of 60 genes related to inflammation, cellular metabolism, carcinogenesis, DNA repair and collagen production.

3.8.1. Transcriptomic profiling of insulation LCPM-exposed cells

Compared to the negative control, incineration LCPM from INS1 (I_INS1), as well as MS-WF, increased the expression of genes involved in chemical carcinogenesis, such as *CYP1A1* (FC (Log_2Fold change) 5.8) and *CYP1B1* (FC 3.08). Moreover, compared to the control, I_INS1 enhanced the expression of genes involved in inflammation, such as *IL1A* (aka IL-1α; FC 2.34), *IL1B* (aka IL-1β; FC 2.61), and *CXCL2* (FC 1.51); cell cycle regulation, such as *CDKN1A* (FC 0.72); and DNA repair, such as *GADD45A* (FC 1.34), and I_INS1 decreased the expression of genes involved in collagen deposition such as *COL5A2* (FC-1.43). In contrast, sanding LCPM M_INS1 or M_INS2 did not induce significant changes of pathways or gene expression compared to MS-WF and the control. GSEA results showed that I_INS1 affected mostly pathways related to *cell cycle* (normalized enrichment score [NES] 2.31) and *semaphorin interactions* (NES −2.18); M_INS1 affected *peptide chain elongation* (NES 2.00) and *developmental biology* (NES −4.88); and M_INS2 affected *mitotic prometaphase* (NES 2.53) and *metabolism of proteins* (NES-4.28) (**SI Excel File 3**).

3.8.2. Transcriptomic profiling of NEC LCPM-exposed cells

Notably, the expression of genes involved in drug metabolism and chemical carcinogenesis such as *CYP1A1* and *CYP1B1* is upregulated in cells treated with all NEC incineration LCPM and MS-WF, compared to control (Fig. 7). Moreover, compared to the control, the incineration LCPM from NECs, regardless of UV-aging, upregulates several genes involved in carcinogenesis (i.e., *FOXC2, FOXE1, ALDH1A3, OSGIN1*), inflammation and angiogenesis (i.e., *CXCL2* (GRO-α), *IL1A* (IL-1α), *IL1B* (IL-1β), *SERPINB2*, *TGFA* (TGF-α), *CXCL8, BMP6*), cell cycle regulation (i.e., *CDKN1A*), collagen production (i.e., *COL16A1*), and cellular metabolism (i.e., *SLC24A3, SLC25A25*). Some genes involved in inflammation and angiogenesis are downregulated (i.e., *CXCL6, PDGFD, BMP3*), as well as genes correlated with a negative cell cycle regulation and carcinogenesis (i.e., *CCNG2, WNT4*). Interestingly, all the NEC LCPM except I_DPP_ACR also downregulate *IDO1* gene expression. Overall, UV-aging of NECs decreases the magnitude of effect of the LCPM on the up- or down-regulation of the genes.

GSEA shows that compared to the control, I_ACR, I_Fe(s)_ACR, I_DPP-ACR, I_UV_ACR, I_UV_Fe(s)-ACR and I_UV_DPP-ACR alter pathways related to the metabolism of proteins (*translation, metabolism of mRNA, peptide chain elongation, signal-recognition particle (SRP) dependent cotranslational protein targeting to membrane*, NES < −3.8). I_ACR also significantly alters the pathways *assembly of the pre-replicative complex* (NES −2.43) and *p53 independent G1-S DNA damage checkpoint* (NES −2.27). I_DPP-ACR alters the *JAK-STAT signaling pathway* (NES 2.14). I_Fe(s)_ACR affects *cell cycle* (NES −4.34) while I_Fe(L)_ACR alters the pathway related to cell respiration, i.e., *respiratory electron transport* (NES −2.79). Enriched pathways are summarized in **SI Excel File 3**.

4. Discussion

The primary motivation of our investigation was to assess the potential health and safety implications of occupational inhalation

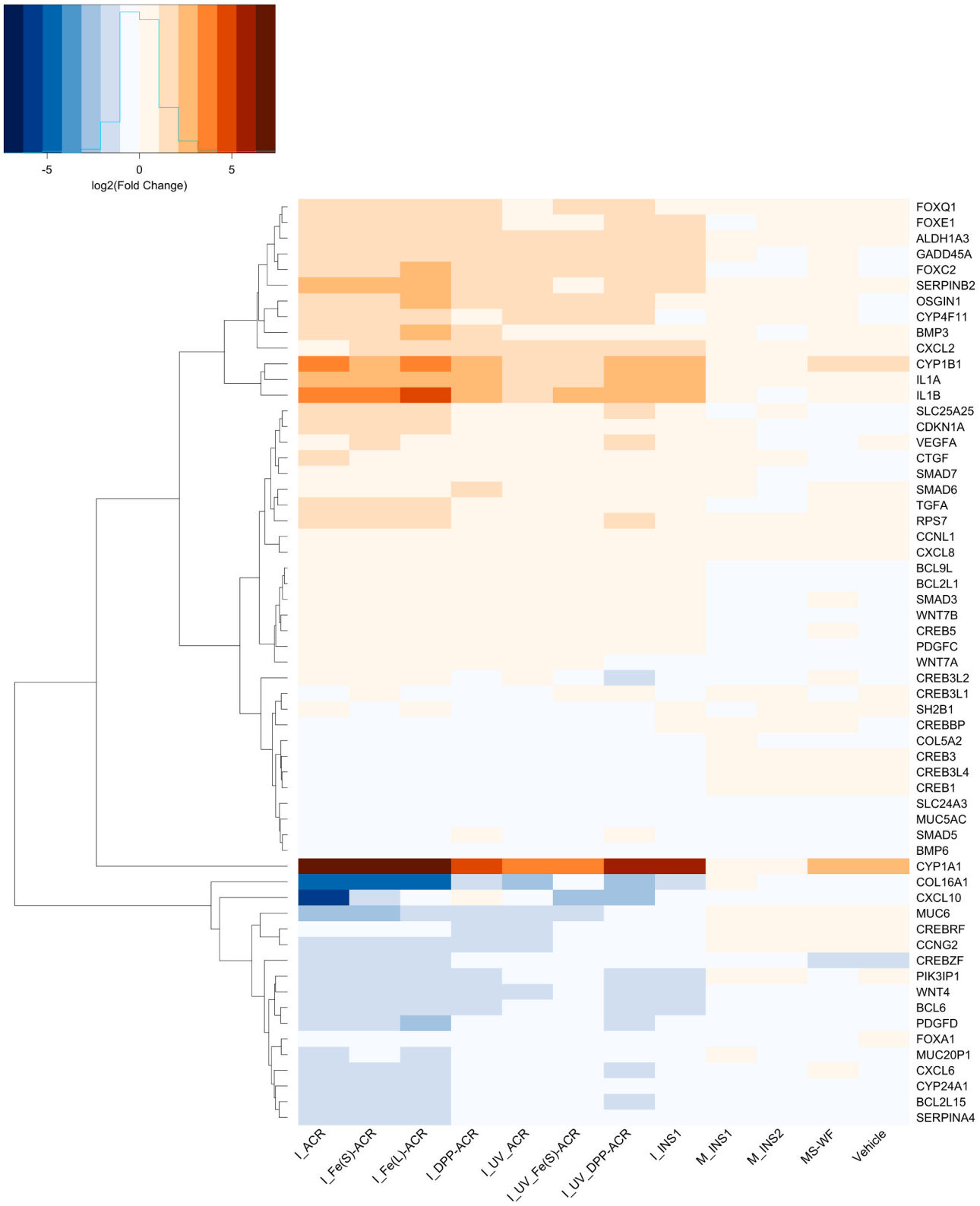

Fig. 7. Heatmap of differential expression results for 60 selected genes from the Calu-3 lung epithelial cell RNA-Seq analysis corresponding to various coating and insulation $LCPM_{2.5}$ exposures at the higher administered dose of 75 μg/mL versus the negative control (culture medium). Shades of red indicate upregulation (Log_2Fold change > 1), while shades of blue indicate downregulation (Log_2Fold change < -1) of the genes, compared to the negative control.

exposures to released particulate matter during multiple lifecycle lysis scenarios of NEBMs during their use phase, environmental weathering, and end-of-life disposal. We focused on two industrially relevant and highly functional classes of building materials, i.e., in-house synthesized NECs with the choice of both inorganic nanofiller (Fe_2O_3) and organic nanofiller (DPP-Red), and the commercially marketed insulations INS1 and INS2, that we confirmed to be nano-enabled (containing various nanoscale metals/metal oxides) through extensive PCM

characterization. The mechanical degradation lifecycle scenario, namely, high-speed sanding, was applied on the insulation blankets under well-controlled operational parameters to assess possible nano-release, physicochemical properties of the released aerosol PM, and its potential toxicological implications for exposed workers. Similarly, we applied the end-of-life thermal decomposition scenario on the insulations and NECs, and further investigated the combined, synergistic effects of sequential lifecycle scenarios by conducting accelerated UV-light weathering of the NECs followed by end-of-life incineration, to answer fundamental questions about the potential airborne release of nanofiller and the important factors (both material-related and lifecycle-specific) governing the released aerosol characteristics and its bioactivity and potential adverse health implications. Here, we discuss the findings of our investigation in a systematic way to address these missing knowledge gaps in the existing literature on the occupational safety of NEBMs. Furthermore, we evaluate if the results to date require further acute/chronic toxicity validation studies on NEBMs and emphasize the importance of including realistic lifecycle exposure and toxicological data as part of occupational risk assessment approaches for advanced building materials.

4.1. Insulation materials: factors governing LCPM release dynamics, physicochemical composition, and in vitro biological effects

4.1.1. Role of matrix in released LCPM characteristics

Our findings point to the strong influencing role of the insulation matrix in determining the released LCPM number concentration, size, and chemical composition, for a given lysis scenario. Comparing two different insulation matrices, INS1 and INS2, the sanded LCPM had slightly different peak aerosol number concentrations and geometric mean optical sizes for the two materials (Fig. 1). The total metal contents of the sanded LCPM, M_INS1 (15.3 wt%) and M_INS2 (32.9 wt%) (Fig. 2E-F), also were in line with the total metal concentrations of the corresponding pristine bulk insulations INS1 (26.1 wt%) and INS2 (37.8 wt%) (Fig. S6), suggesting that the matrix composition governs the sanding LCPM chemistry, and the released metallic nanoparticles are largely encapsulated within the sanded matrix fragments. Similarly, INS1 and INS2 matrices behaved drastically different during the incineration scenario. TD of INS1 led to a high emitted aerosol number concentration ($\sim 10^8$ particles/cm^3, Fig. 3 A) and a $PM_{2.5}$ aerosol yield of 0.6 wt% (Table S2), whereas INS2 underwent minimal or no TD at all, as evident from no change in aerosol concentration from the baseline and a very low measured $PM_{2.5}$ yield of 0.02 wt%. The higher combustibility of the INS1 insulation compared to INS2 is likely attributed to the presence of a significant concentration (10–20 wt%) of the thermoplastic polyethylene terephthalate (PET) in the INS1 matrix, as disclosed in the manufacturer-provided MSDS composition for INS1 (Table 1). On the other hand, there is no combustible carbon-based polymer in the INS2 as per the MSDS, but only silica-based and metallic ingredients, thus explaining its excellent thermal resistance even at 850 °C. Although the TGA-GC-MS spectra of evolved volatile compounds from INS2 points to the presence of siloxane (-Si-O-Si-), siloxy (R_3-Si-O-), or methylsilyl (R_3-Si-) functional groups in the INS2 matrix, these organosilicon compounds can act as flame retardants and suppress the thermal decomposition of the INS2 matrix (Han et al., 2014). The chemical composition of the incineration LCPM from INS1 and INS2 also differed significantly (Fig. 4A-B), with a higher released metal content in I_INS2 (8.4 wt%) than I_INS1 (1.2 wt%), in line with the higher metal content of the pristine INS2 (37.8 wt%) compared to INS1 (26.1 wt%). This indicates that even though the INS2 matrix did not sufficiently thermally degrade, the incineration process resulted in some of the nanoscale metals/metal oxides incorporated in the matrix to escape into the released aerosol PM. Thus, the physicochemical makeup of the insulation matrices played a critical role in determining the extent of airborne nano-release and therefore the elemental composition of the released incineration LCPM. Our previous TD investigations with nano-enabled thermoplastics also highlighted the important role of the polymer matrix in governing the total released LCPM number concentrations and the overall LCPM chemical composition. For example, in terms of organic/elemental carbon content, the TD LCPM consisted of 99 wt% organic carbonaceous compounds for a given matrix irrespective of the nanofiller type or its weight loading in the polymer matrix (Sotiriou et al., 2015, 2016). The released LCPM nanoparticle number concentration and the mean aerosol size during TD also differed significantly between the investigated polymer matrices (polyethylene (PE), polypropylene (PP), polycarbonate (PC), and ethyl-vinyl acetate (EVA)), confirming that the bulk matrix degradation during the lysis scenarios contributes the most to the LCPM release dynamics (Sotiriou et al., 2015, 2016; Singh et al., 2016).

4.1.2. Effect of lifecycle lysis scenario on released LCPM characteristics

It is clear from our findings and even intuitive that the extent of lifecycle degradation of the NEBM changes the LCPM release dynamics and PCM properties of the LCPM. For example, while sanding of the insulation INS1 resulted in a peak aerosol number concentration of only ~30,000 particles/cm^3, thermal degradation of INS1 resulted in hundreds of millions of particles/cm^3. This is easily explained as the total energy input into a high-temperature incineration process is much higher than what is imparted by even a high-speed sanding machine, thereby resulting in a higher degree of disintegration of the matrix, leading to the production of a more concentrated aerosol (Duncan, 2015). Furthermore, the LCPM generated by the incineration of insulation INS1 had a much lower inorganic (metallic) content compared to the sanding LCPM, which could be explained by the relatively high fraction of carbonaceous compounds in the incineration LCPM (Singh et al., 2016, 2019), whereas the sanding LCPM resembled more closely the physicochemical composition of the pristine insulation matrix, and thus had a high inorganic metallic content.

4.1.3. Role of matrix and lifecycle lysis scenario in LCPM-induced bioactivity, inflammation, and gene expression

In vitro toxicological assessment of the sanding and incineration LCPM from the insulation materials on the Calu-3 lung epithelial cells using the cell viability, metabolic activity, and oxidative stress endpoints indicated that these insulations, as well as the comparator MS-WF, were non-cytotoxic (Fig. 5) irrespective of the matrix or the lysis scenario. In addition to basic cytotoxicity assays, further insight into the acute inflammatory effects of the insulation LCPM was gained through a comprehensive analysis of 48 inflammatory cytokines, chemokines, and growth factors. Calu-3 human lung epithelial cells exposed to LCPM produced from different manipulations of the same insulation material (INS1), i.e., sanding and incineration, exhibited two different inflammatory phenotypes. While LCPM produced by incineration of INS1 (I_INS1) stimulated the release of pro-angiogenic and pro-inflammatory cytokines, such as PDGF-AA, TGF-α, GM-CSF, IL-6, (Fig. 6), IFN-γ, and IL-1α (Fig. S15), particles released by sanding of the same material (M_INS1) promoted only the upregulation of some pro-inflammatory mediators, such as TGF-α, GM-CSF, IL-6, (Fig. 6), while inhibiting the pro-fibrotic mediators, VEGF, PDGF-AA, PDGF-AB/BB, and FGF-2 (Fig. 6). In sharp contrast, none of these effects were observed when cells were stimulated with LCPM generated from sanding of a different insulation material (M_INS2) or the comparator material MS-WF.

These findings were supported by transcriptomic results obtained with RNA-Seq. Calu-3 human lung epithelial cells exposed to LCPM produced by incineration of insulation material (I_INS1) showed upregulation of genes related to inflammation, such as *IL1A* (the gene encoding IL-1α), *IL1B* (the gene encoding IL-1β), *CXCL2*, *CTGF*, mirroring the release of their inflammatory cytokine protein products (Fig. 7). More importantly, the altered expression of genes and pathways involved in drug metabolism, DNA repair, and cell cycle dysfunction is an indication of the possible chemical carcinogenic effect of this specific insulation incineration LCPM (Oliveira et al., 2007; Anwar-Mohamed

et al., 2009). On the other hand, cells exposed to LCPM from sanding of INS1 and INS2 (M_INS1 and M_INS2) exhibited an altered expression of pathways related to the cell metabolism of proteins, lipids, and glucose, and cell junction organization **(SI Excel File 3)**.

These findings clearly indicate that the physicochemical properties of the insulation matrix, as well as the subsequent lifecycle lysis scenario, dictate the PCM properties of the LCPM emissions, which consequently affect the cellular inflammation response. Although both INS1 and INS2 and their respective sanding LCPM contain a high inorganic (heavy metals) content with similar elemental profiles, INS1 is known to contain ~10–20% by weight of PET plastic (as disclosed in MSDS) in addition to other organic polymers estimated from TGA-GC-MS data such as poly(alpha-methylstyrene) (PAMS), that could explain the higher inflammatory, fibrotic and carcinogenic potential of the LCPM released from sanding of INS1 compared to INS2 on lung epithelial cells (Morgan et al., 1999). Furthermore, incineration LCPM appears to be more inflammogenic compared to sanding LCPM from the insulation (INS1), which could be attributed to the presence of a complex mixture of organic compounds adsorbed to the surface of incineration LCPM that are typically produced as byproducts of combustion, such as toxic and carcinogenic PAHs (Singh et al., 2017; Vejerano et al., 2013, 2014), in addition to other potentially toxic volatile organic compounds identified in the TGA spectra such as halogenated organics (Li et al., 2019).

4.2. NECs: factors governing LCPM release dynamics, physicochemical composition, and in vitro biological effects

4.2.1. Effect of nanofiller type on released LCPM characteristics

The role of the nanofiller type on the released LCPM physicochemical characteristics was evaluated during the incineration of the NECs with different nanofiller chemistries. Significant differences were observed in the released LCPM number concentration and mean aerosol mobility size between the nano-coatings with Fe_2O_3 and DPP nanofillers with a higher emitted nanoparticle number concentration and a higher LCPM aerosol size observed in the presence of Fe_2O_3 nanofiller (Fig. 3). These differences in particle concentration and size between the different nanofiller types could be due to the catalytic nature of Fe_2O_3 that can promote the growth and agglomeration of combustion-generated carbonaceous particles on its surface in the released aerosol (Mahinroosta, 2013), whereas most of the organic nanofiller DPP-Red is expected to be burnt off during the high incineration temperatures, thus not providing the additional particle surface area to promote PM-producing combustion reactions. Also, it was observed that the signature elements Fe and Cl corresponding to Fe_2O_3 and DPP-Red nanofillers respectively were released in the incineration $PM_{2.5}$ in small concentrations, therefore, due to the possible release of associated nanofillers in the aerosol, the physicochemical characteristics of the released LCPM are determined at least in part by the nanofiller chemistry, if not as much by the bulk matrix (acrylic polymer) of the coating. This release of inorganic nanofillers (Fe_2O_3, TiO_2) in the aerosol was also observed during our previous TD investigations on thermoplastic polymers containing these nanofillers at comparable mass loadings (PE-5% Fe_2O_3, EVA-5% TiO_2) (Sotiriou et al., 2016; Singh et al., 2016), further affirming that inorganic nanofillers are likely to be released in the aerosol during thermal decomposition of the polymer matrix and thus influence the physicochemical characteristics of the LCPM. Not only the nanofiller type, but the size of the Fe_2O_3 nanofiller also affected the released LCPM physicochemical characteristics. The NEC with the larger size Fe_2O_3 nanofiller (mean diameter = 150 nm) displayed a smaller TD LCPM mobility size of 70 nm compared to the 102 nm LCPM size for the smaller size Fe_2O_3 nanofiller (mean diameter = 37 nm). The explanation for this could also have to do with the significantly more specific surface area offered by the smaller size nanofiller compared to the larger size one (for the same mass loading of 1.5 wt%) during the TD, thereby accelerating the nucleation, growth, and agglomeration of organic soot particles and resulting in a larger LCPM size. Our previous systematic TD studies also revealed significant effects of nanofiller physical properties on the released LCPM, for example, when TiO_2 nanofiller loadings in a given thermoplastic polymer matrix (EVA) were varied between 2 and 15 wt%, the mean mobility size distribution of the released aerosol shifted markedly (Singh et al., 2016).

4.2.2. Effect of environmental weathering on released LCPM characteristics

Another important lifecycle scenario comparison that our study allows for is investigating the effect of sequential lifecycle stresses imposed on NEBMs on the released LCPM characteristics, i.e., UV-aging followed by incineration of NECs compared to NEC incineration alone. For the three coatings (ACR, Fe(s)-ACR, and DPP-ACR) investigated for these combined scenarios, it was observed that the released LCPM physicochemical characteristics did not differ significantly between the incineration and UV/incineration scenarios. The released LCPM number concentrations, mobility sizes, and the LCPM elemental compositions were similar for the two groups of scenarios (Figs. 3 and 4). A possible reason for this could be that the UV-aging of NECs for 3 months did not significantly transform the bulk physicochemical composition of the acrylic polymer matrix, even though there could have been surface-level physicochemical degradation and structural changes (e.g., cracking) (Wohlleben et al., 2017) in the NEC due to the high-intensity UV light exposure. As a result, we believe that the subsequent highly destructive TD process at the high temperature of 850 °C after UV-aging has assimilated the minor changes induced between the unaged and UV-aged matrices in terms of the overall released LCPM physicochemical characteristics.

4.2.3. Effect of LCPM physicochemical composition on in vitro toxicity

In vitro cytotoxicity assessment of the incineration and UV/incineration LCPM from the NECs on the Calu-3 lung epithelial cells indicated that these NECs exhibit minimal bioactivity (Fig. 5). Incineration LCPM from the unaged matrix-only and Fe_2O_3 nanofiller (both large and small) containing acrylic coatings induced a significantly higher cell metabolic activity and oxidative stress (only for large Fe_2O_3) at the higher LCPM dose of 75 μg/mL (Fig. 5E, F), but not for the corresponding UV-aged coatings, indicating that bioactivity is dose-dependent and specific to the matrix, nanofiller composition, and total lifecycle stresses undergone by the NEBM. The effect of Fe_2O_3 nanofiller on increased cytotoxicity and bioactivity of LCPM in small airway epithelial cells was previously demonstrated in our study on the incineration of thermoplastic PE containing the Fe_2O_3 nanofiller at 5 wt% loading (Watson-Wright et al., 2017). Also, while the incineration LCPM from the UV-aged DPP-ACR increased metabolic activity at the higher dose, no significant effect was observed for LCPM from the unaged DPP-ACR (Fig. 5E), which could partly be attributed due to the slightly higher elemental concentration of Cl in the I_UV_DPP-ACR (0.3 at%, Fig. 4I) LCPM compared to I_DPP-ACR (0.14 at%, Fig. 4H). Therefore, the presence of released nanofiller in the LCPM appears to be one of the important driving factors in determining its bioactivity or toxicity. Our previously published in vitro toxicity studies with TD LCPM from nano-enabled thermoplastics confirmed that the presence of nanofiller enhances the toxicological profile of the released LCPM where we investigated the effects of nanofillers such as CNT, TiO_2, and Fe_2O_3 at various mass loadings in different polymer matrices (PU, EVA, PE) (Singh et al., 2016). The incineration LCPM is known to contain a large fraction of complex organic compounds and their synergistic interactions with released nano-metals such as Fe and Ti having a large specific surface area and combustion catalytic properties (Kohga and Togo, 2020) could exacerbate the LCPM toxicological response, for example through the formation of large molecular weight and toxic PAHs in the released LCPM, as we found in our previous investigations (Chalbot et al., 2017; Singh et al., 2017).

4.2.4. Effect of LCPM physicochemical composition on acute inflammation

Human lung epithelial cells exposed to LCPM emissions from

incineration of nano Fe_2O_3-enabled coating materials (I_Fe(s)-ACR and I_Fe(L)-ACR) exhibited the strongest secretion of inflammatory cytokines and growth factors, substantially involved in the development of inflammation and pulmonary fibrosis, such as VEGF, PDGF-AA, TGF-α, TNFα, TNFβ, and GM-CSF, and strong inhibition of IP-10 (Fig. 6), while interestingly, the corresponding incineration LCPM from UV-aged NECs, as well as MS-WF, had no pro-inflammatory effect on lung epithelial cells compared to untreated cells. The presence of iron oxide nanofiller in the NECs is a potential risk factor for the induction of acute and chronic inflammatory response and pulmonary fibrosis due to potential inhalation of released Fe in the incinerated LCPM in the occupational environment, principally due to iron oxide nanoparticle induced oxidative stress, as reported in the very few available studies performed in mice and rats (Park et al., 2015, 2010; Srinivas et al., 2012; Ban et al., 2013; Gustafsson et al., 2015; Sadeghi and Espanani, 2015; Szalay et al., 2012; Zhu et al., 2008). In agreement with the current literature, we found that LCPM released from the incineration of nano Fe_2O_3-enabled coating materials induced oxidative stress, inflammatory response, and pro-fibrotic phenotype in lung epithelial cells. It is important to mention that MS-WF also contains iron oxide, which has been hypothesized to govern the inflammatory response and pulmonary fibrosis in welders after long-term exposure (Andujar et al., 2014). However, despite the presence of Fe_2O_3, no signs of acute inflammation have been reported in vivo or in humans exposed to MS-WF.

Comparatively, the LCPM released from the incineration of nano DPP-Red-enabled coating materials (I_DPP-ACR) stimulated the secretion of pro-inflammatory cytokines, such as GM-CSF, TNFα, IL-6, IL-18, IL-1α, IFN-γ, while in the presence of prior UV-aging, only the secretion of TNFβ and IL-6 was induced (Fig. 6 and S15). Regardless of prior UV-aging, cells exposed to incineration LCPM from DPP-enabled NECs released a higher concentration of pro-fibrotic markers, such as PDGF-AA and TGF-α, accompanied by IP-10 suppression (Fig. 6), when compared to MS-WF or control. As for the pristine DPP-Red nanofiller, the toxicological findings are more often reported in regulatory dossiers than in academic literature. A recent review has compared the toxicity of several organic pigments including DPP-Red, and points to the role of pigment solubility in water/octanol as a predictor of its potential toxicity and systemic uptake, which would classify DPP-Red as generally inert due to its poor solubility (<0.1 mg/L) (Stratmann et al., 2020). However, in a recent short-term inhalation study (Hofmann et al., 2016) conducted on Wistar rats, exposure to a high DPP-Red nanoparticle concentration of 30 mg/m^3 for 6 h/day for 5 days caused pigment deposits and phagocytosis by alveolar macrophages, slight hypertrophy/hyperplasia of the bronchioles and alveolar ducts and marginal effects on broncho-alveolar lavage fluid, but without evidence of systemic inflammation. However, such chlorinated organic pigments might not be released in their pristine state into the aerosol but may undergo significant PCM transformations during incineration at high temperatures and thus cause the formation of chlorinated organics such as chloroalkanes and chlorinated PAHs in addition to other toxic combustion byproducts such as hydrogen chloride, resulting in adverse pulmonary effects (Huggett and Levin, 1987; Blankenship et al., 1994).

Interestingly, although the physicochemical properties of the incineration LCPM did not differ markedly between the unaged and UV-aged NECs, it seems that prior UV-aging of the NECs before incineration completely abolished the bioactive and inflammogenic potential of the nano Fe_2O_3-enabled coatings. This difference was also found for cells exposed to LCPM released from incineration of the control ACR coating vs. the corresponding UV-aged ACR coating. Although we did not investigate possible mechanisms to explain this UV-aging effect on LCPM bioactivity and inflammogenicity in the current study, one hypothesis is that the accelerated UV weathering of the coatings induced free radical-mediated photochemical oxidation, matrix degradation, and breaking of polymer chains of the acrylic polymer (Wohlleben et al., 2017; Zepp et al., 2020; Yousif and Haddad, 2013), thus resulting in a significant PCM transformation of the coatings and hence the properties of the released incineration LCPM. In the presence of the photocatalytic Fe_2O_3 nanofiller in the acrylic matrix, this photo-oxidation would be likely accelerated (Pagnin et al., 2020; Pintus et al., 2016; Mishra and Chun, 2015), further causing structural and chemical changes in the NEC, and subsequently reflecting in the toxicological properties of the incineration LCPM. In the case of DPP-Red nanofiller, however, although the prior UV-aging on DPP-Red-enabled acrylic coating abolished the secretion of some inflammatory cytokines such as GM-CSF, TNF-α, IL-1α, IL-18, and IFNγ, it did not affect the release of cytokines such as PDGF-AA, TGF-α, and IL-6 which were still upregulated similarly to the unaged DPP-ACR. A possible explanation for this phenomenon is that DPP organic pigments are known to be strong UV light absorbers and thus offer good UV stability to polymers (Bao et al., 2020; Zeng et al., 2018), thereby inhibiting their photochemical degradation from prolonged UV exposure. Therefore, the incineration LCPM PCM and toxicological properties of the UV-aged DPP-ACR might not be significantly different from the unaged DPP-ACR due to the UV-protective effects of DPP-Red.

Notably, incineration LCPM from all NEC resulted in a significant decrease in IP-10, MDC, and RANTES secretion. IP-10 is a selective chemoattractant for both activated type 1T lymphocytes and natural killer cells, and an angiostatic chemokine that regulates the endothelial tube formation, contrasting the pro-angiogenetic role of VEGF and PDGF, thus its downregulation leads to pathologic conditions such as idiopathic pulmonary fibrosis (IPF) (Cui et al., 2010; Bodnar et al., 2006; Luster et al., 1995; Yates-Binder et al., 2012; Keane et al., 1997). Both MDC and RANTES chemokines' primary source is represented by smooth muscle cells and bronchiolar epithelium and their function is primarily recruitment of macrophages and eosinophils, thus involvement in eosinophilia and airway hyper-reactivity (Lloyd, 2002). Further studies are necessary to investigate the role of monocytes/macrophages and eosinophils in the response to these complex LCPM.

Altogether, our findings indicate that given the multiplicity of metallic and organic species in the released LCPM from NEBMs during different lifecycle scenarios, it is not always possible to define which specific chemical component in the LCPM drives the lung alterations, but it is the synergism among the various chemical species, more than the effect of a single heavy metal or organic compound, that governs the acute toxicity and inflammogenic potential of the inhaled LCPM in the lung. Thus, altogether, these data suggest that the physicochemical composition of the LCPM that is governed by the matrix/nanofiller chemistry and the specific lifecycle lysis scenario(s) plays a crucial role in the development of adverse pulmonary conditions such as acute and chronic lung inflammation, neoangiogenesis, progressive collagen deposition, and subsequently secondary pulmonary fibrosis.

4.2.5. *Effect of LCPM physicochemical composition on gene expression*

Consistent with our in vitro bioactivity and acute inflammatory response data, changes in gene expression of lung epithelial cells exposed to LCPM generated from NEC incineration highlighted that the more bioactive LCPM were I_ACR, I_Fe(s)-ACR, I_Fe(L)-ACR, I_DPP-ACR, and I_UV_DPP-ACR, further confirming the suppressive effect of UV-aging on NEC LCPM bioactivity. Indeed, these specific LCPM modulated genes involved in drug metabolism, carcinogenesis, inflammation, angiogenesis, cell cycle regulation, collagen production, and cellular metabolism.

Even though it is not possible to determine specific disease mechanisms from our gene expression results of in vitro exposures to the different LCPM tested, our results indicate that in vivo studies in exposed workers could focus on increased risk of specific diseases, such as metabolic disease and cancer. Indeed, our previous studies have demonstrated that inhalation of printed-emitted nanoparticles perturbed transcriptional activities associated with cardiovascular dysfunction, metabolic syndrome, and neural disorders at every observed time point in both rat lung and blood after 21 days of exposure (Guo et al., 2019). A similar systemic effect was observed in another

RNA-Seq study performed by our group of blood samples of workers exposed to ENMs used in toner-based printing equipment in two printing companies in Singapore, in which we found altered gene expression and pathways related to inflammatory and immune responses, metabolism, cardiovascular impairment, neurological diseases, oxidative stress, physical morphogenesis/deformation, and cancer, when compared with control peers (office workers) (Guo et al., 2020). In this view, deeper mechanistic and omics studies on a controlled cohort of construction workers are warranted in order to assess potential risk for cancer and other systemic diseases as a result of acute and chronic exposures to LCPM generated from NEBMs and other emerging advanced building materials.

5. Conclusions

This study provides important data on the occupational health and safety implications of exposures to NEBMs during the various degradation scenarios that they undergo during their lifecycle by utilizing an industrially relevant NEBM panel of two commercially available insulation materials and in-house synthesized nano-coatings with different nanofillers (inorganic and organic). It was demonstrated that commercially procured insulation materials were indeed nano-enabled building materials containing a variety of nanoscale metals/metal oxides including several heavy metals with known toxicity. We investigated three categories of lifecycle scenarios on the NEBM panel, i.e., mechanical degradation (sanding) (on insulation materials), thermal decomposition (or incineration) (on insulation materials and nano-coatings), and a combined, sequential lifecycle scenario of environmental weathering (simulated by accelerated UV-aging) followed by thermal decomposition (on nano-coatings), to assess important factors determining the LCPM release dynamics, its physicochemical composition, and potential inhalation toxicological effects.

As for the insulation materials, the composition of the matrix played a significant role in determining the LCPM release dynamics and its physicochemical properties, for a given lysis scenario. During sanding of both insulations, metallic nanoparticles were released primarily as part of the submicron and micron-sized sanded matrix fragments and the elemental composition of the sanded LCPM reflected that of the pristine bulk insulation material. During incineration, only one of the insulation materials (INS1) underwent significant thermal degradation (likely due to the presence of the thermoplastic PET in the matrix) and emitted a high nanoparticle concentration that was nearly 4 orders of magnitude higher than the sanding scenario. However, both insulations released metallic species into the incineration LCPM corresponding to the nano-metals in the pristine insulations, indicating that nano-release could occur at high temperatures even without sufficient degradation of the insulation matrix. Insulation LCPM from either sanding or incineration was not cytotoxic, however, significant acute inflammatory effects and increased expression of genes related to chemical carcinogenesis and inflammation were observed for the LCPM from insulation INS1 compared to INS2 and the comparator MS-WF, and more so for the incineration LCPM compared to sanding LCPM, suggesting the importance of the synergy between the matrix chemistry and lysis scenario in determining the potential adverse biological effects of released LCPM.

As for the NECs, for a given polymer matrix (i.e., acrylic), the nanofiller physicochemical properties affected the released LCPM number concentration and mean aerosol size during incineration. The signature elemental species corresponding to both the inorganic (Fe from Fe_2O_3) and organic (Cl from DPP-Red) nanofillers were released in the LCPM, providing evidence of nanofiller release, although at high decomposition temperatures the released nanofillers could be physicochemically transformed. The LCPM release dynamics and physicochemical properties did not differ significantly between the unaged and prior UV-aged NECs, suggesting that the high energy incineration process dominated the LCPM release profiles. Although not cytotoxic, incineration LCPM from the unaged NECs containing Fe_2O_3 nanofiller showed dose-dependent bioactivity via the increased metabolic activity of the lung epithelial cells at the higher LCPM dose. Incineration LCPM from all unaged NECs exhibited a marked increase in pro-inflammatory, pro-fibrotic, and pro-angiogenic biomarkers as well as upregulation of several genes involved in carcinogenesis, inflammation, and angiogenesis compared to the negative control or the comparator MS-WF particles, but this acute inflammatory effect was greatly attenuated for the UV-aged NECs, suggesting the important role of outdoor environmental weathering on LCPM toxicological properties.

Further in vitro and in vivo inhalation studies are warranted to validate acute/chronic toxicological effects and investigate potential systemic disease mechanisms as a result of inhalation exposures to real-world LCPM exposures from such NEBMs. Occupational risk assessors in industry and governmental agencies need to take into account realistic lifecycle-specific exposure and toxicological data from representative families of NEBMs in order to adequately assess worker health risks, rather than relying on permissible and recommended exposure limits (PELs/RELs) determined by Occupational Safety and Health Administration (OSHA)/NIOSH for individual ENMs or total nuisance dust, which are based on hazards of the pristine materials and not on the lifecycle-transformed properties of released nanomaterials (Schulte et al., 2018). Such systematic exposure generation and toxicological characterization studies on advanced building materials also promise to provide useful scientific feedback to industrial manufacturers that could guide the development of safer-by-design construction materials that minimize the release of embedded nanomaterials and inhalable PM under various lifecycle conditions. Lastly, our study's findings emphasize the importance of ensuring the adequate level of personal protective equipment and exposure engineering controls for construction workers that are tailored to specific handling/manipulation procedures (e.g., drilling, burning, etc.) and inherent properties/hazards of building materials, rather than non-specific, general safety practices.

Supporting information

SI file contents: pictures of coatings and insulations, picture and schematic of sanding setup, schematic of the incineration setup, schematic of the TSI fluidized bed aerosol generator, SEM/TEM/EDX and ICP-MS data on pristine insulation materials, aerodynamic size distribution of resuspended sanded insulation dusts, EDX spectra of sanded insulation dusts, TGA-FTIR-GC-MS spectra of insulation materials, selected inflammatory biomarkers up/down-regulated by insulations/coatings LCPM, detailed PCM characterization of coating nanofillers (methods and results), incineration PM and residual ash yields, DLS colloidal characterization of LCPM suspensions, technical details on nanocoating synthesis, methodological details on ICP-MS analysis of pristine materials and LCPM particles, methodological details on TGA-FTIR-GC-MS analysis of LCPM, justification for cellular doses, Excel File 1 (ICP-MS mass concentrations and standard deviations), Excel File 2 (significant genes), Excel File 3 (pathway analysis).

CRediT authorship contribution statement

Dilpreet Singh: Conceptualization, Methodology, Validation, Formal analysis, Investigation, Writing – original draft, Writing – review & editing, Visualization. **Antonella Marrocco:** Validation, Formal analysis, Investigation, Writing – original draft, Writing – review & editing, Visualization. **Wendel Wohlleben:** Conceptualization, Investigation, Resources, Writing – review & editing. **Hae-Ryung Park:** Software, Validation, Formal analysis, Writing – review & editing, Visualization. **Avantika R. Diwadkar:** Software, Validation, Formal analysis, Writing – review & editing. **Blanca E. Himes:** Software, Validation, Formal analysis, Writing – review & editing. **Quan Lu:** Conceptualization, Methodology, Writing – review & editing. **David C. Christiani:** Conceptualization, Methodology, Resources, Writing – review & editing, Supervision, Funding acquisition. **Philip Demokritou:**

Conceptualization, Methodology, Writing – review & editing, Supervision, Project administration, Funding acquisition.

Declaration of Competing Interest

The authors declare that they have no known competing financial interests or personal relationships that could have appeared to influence the work reported in this paper.

Acknowledgements

This investigation was made possible by Grant No. T42 OH008416 from the US National Institute for Occupational Safety and Health (NIOSH). Its contents are solely the responsibility of the authors and do not necessarily represent the official views of the NIOSH. Additionally, research was supported by the HSPH-NIEHS Nanosafety Center, a member of the Nanotechnology Health Implications Research (NHIR) consortium. The library preparation and RNA-sequencing were made possible by Grant No. P30ES000002 from the Integrated Health Sciences Facility (IHSFC) of the Harvard NIEHS Center for Environmental Health. The engineered nanomaterial characterization work was performed in part at the Harvard Center for Nanoscale Systems (CNS), a member of the National Nanotechnology Infrastructure Network (NNIN), which is supported by the US National Science Foundation under NSF award no. ECS-1541959. The ICP-MS analysis was performed by the Wisconsin State Laboratory of Hygiene based at the University of Wisconsin-Madison. AM acknowledges funding from the National Institutes of Health (NIH) T32 training grant. WW acknowledges partial funding from H2020 Grant Agreement 953183 (HARMLESS).

Appendix A. Supporting information

Supplementary data associated with this article can be found in the online version at doi:10.1016/j.jhazmat.2021.126771.

References

GSEA | MSigDB | MSigDB Collections, (n.d.). https://www.gsea-msigdb.org/gsea/msigdb/collections.jsp (Accessed 15 April 2021).

ISO - ISO 4892–2:2013 - Plastics — Methods of exposure to laboratory light sources — Part 2: Xenon-arc lamps, (n.d.). https://www.iso.org/standard/55481.html (Accessed 22 April 2021).

Al-Bayati, A.J., Al-Zubaidi, H.A., 2018. Inventory of nanomaterials in construction products for safety and health. J. Constr. Eng. Manag. 144, 06018004 https://doi.org/10.1061/(ASCE)CO.1943-7862.0001547.

Anders, S., Pyl, P.T., Huber, W., 2015. HTSeq-a python framework to work with high-throughput sequencing data. Bioinformatics 31, 166–169. https://doi.org/10.1093/bioinformatics/btu638.

S. Andrews, Babraham Bioinformatics - FastQC A Quality Control tool for High Throughput Sequence Data, (n.d.). https://www.bioinformatics.babraham.ac.uk/projects/fastqc/ (Accessed 15 April 2021).

Andujar, P., Simon-Deckers, A., Galateau-Sallé, F., Fayard, B., Beaune, G., Clin, B., Billon-Galland, M.-A., Durupthy, O., Pairon, J.-C., Doucet, J., 2014. Role of metal oxide nanoparticles in histopathological changes observed in the lung of welders. Part. Fibre Toxicol. 11, 23.

Anjilvel, S., 1995. A multiple-path model of particle deposition in the rat lung. Fundam. Appl. Toxicol. 28, 41–50. https://doi.org/10.1006/FAAT.1995.1144.

Antonini, J.M., Lawryk, N.J., Krishna Murthy, G.G., Brain, J.D., 1999. Effect of welding fume solubility on lung macrophage viability and function in vitro. J. Toxicol. Environ. Heal. Part A 58, 343–363. https://doi.org/10.1080/009841099157205.

Antonini, J.M., Zeidler-Erdely, P.C., Young, S.H., Roberts, J.R., Erdely, A., 2012. Systemic immune cell response in rats after pulmonary exposure to manganese-containing particles collected from welding aerosols. J. Immunotoxicol. 9, 184–192. https://doi.org/10.3109/1547691X.2011.650733.

Anwar-Mohamed, A., Elbekai, R.H., El-Kadi, A.O.S., 2009. Regulation of CYP1A1 by heavy metals and consequences for drug metabolism. Expert Opin. Drug Metab. Toxicol. 5, 501–521. https://doi.org/10.1517/17425250902918302.

Aytac, Z., Huang, R., Vaze, N., Xu, T., Eitzer, B.D., Krol, W., MacQueen, L.A., Chang, H., Bousfield, D.W., Chan-Park, M.B., Ng, K.W., Parker, K.K., White, J.C., Demokritou, P., 2020. Development of biodegradable and antimicrobial electrospun zein fibers for food packaging. ACS Sustain. Chem. Eng. 8, 15354–15365. https://doi.org/10.1021/acssuschemeng.0c05917.

Ban, M., Langonné, I., Huguet, N., Guichard, Y., Goutet, M., 2013. Iron oxide particles modulate the ovalbumin-induced Th2 immune response in mice. Toxicol. Lett. 216, 31–39.

Bao, W.W., Li, R., Dai, Z.C., Tang, J., Shi, X., Geng, J.T., Deng, Z.F., Hua, J., 2020. Diketopyrrolopyrrole (DPP)-based materials and its applications: a review. Front. Chem. 8, 679. https://doi.org/10.3389/fchem.2020.00679.

Barnett, D.W., Garrison, E.K., Quinlan, A.R., Strömberg, M.P., Marth, G.T., 2011. Bamtools: a C++ API and toolkit for analyzing and managing BAM files. Bioinformatics 27, 1691–1692. https://doi.org/10.1093/bioinformatics/btr174.

Bello, D., Wardle, B.L., Zhang, J., Yamamoto, N., Santeufemio, C., Hallock, M., Virji, M. A., 2013. Characterization of exposures to nanoscale particles and fibers during solid core drilling of hybrid carbon nanotube advanced composites. Int. J. Occup. Environ. Health 16, 434–450. https://doi.org/10.1179/107735210799159996.

Blankenship, A., Chang, D.P.Y., Jones, A.D., Kelly, P.B., Kennedy, I.M., Matsumura, F., Pasek, R., Yang, G.S., 1994. Toxic combustion by-products from the incineration of chlorinated hydrocarbons and plastics. Chemosphere 28, 183–196. https://doi.org/10.1016/0045-6535(94)90212-7.

Bodnar, R.J., Yates, C.C., Wells, A., 2006. IP-10 blocks vascular endothelial growth factor-induced endothelial cell motility and tube formation via inhibition of calpain. Circ. Res. 98, 617–625. https://doi.org/10.1161/01.RES.0000209968.66606.10.

F.R. Cassee, J.I. Freijer, R. Subramaniam, B. Asgharian, F.J. Miller, L. Van Bree, P.J.A. Rombout, RIVM report 650010 018 Development of a model for human and rat airway particle deposition: implications for risk assessment, 1999.

Chalbot, M.C.G., Pirela, S.V., Schifman, L., Kasaraneni, V., Oyanedel-Craver, V., Bello, D., Castranova, V., Qian, Y., Thomas, T., Kavouras, I.G., Demokritou, P., 2017. Synergistic effects of engineered nanoparticles and organics released from laser printers using nano-enabled toners: potential health implications from exposures to the emitted organic aerosol. Environ. Sci. Nano 4, 2144–2156. https://doi.org/10.1039/c7en00573c.

Clausen, P.A., Kofoed-Sørensen, V., Nørgaard, A.W., Sahlgren, N.M., Jensen, K.A., 2019. Thermogravimetry and mass spectrometry of extractable organics from manufactured nanomaterials for identification of potential coating components. Mater. (Basel) 12. https://doi.org/10.3390/ma12223657.

Cohen, J.M., Teeguarden, J.G., Demokritou, P., 2014. An integrated approach for the in vitro dosimetry of engineered nanomaterials. Part. Fibre Toxicol. 11, 20. https://doi.org/10.1186/1743-8977-11-20.

Cui, A., Anhenn, O., Theegarten, D., Ohshimo, S., Bonella, F., Sixt, S.U., Peters, J., Sarria, R., Guzman, J., Costabel, U., 2010. Angiogenic and angiostatic chemokines in idiopathic pulmonary fibrosis and granulomatous lung disease. Respiration 80, 372–378. https://doi.org/10.1159/000245332.

Das, B.B., Mitra, A., 2014. Nanomaterials for construction engineering-a review. Int. J. Mater. Mech. Manuf. 2, 41–46. https://doi.org/10.7763/IJMMM.2014.V2.96.

DeLoid, G.M., Cohen, J.M., Pyrgiotakis, G., Demokritou, P., 2016. An integrated dispersion preparation, characterization and in vitro dosimetry methodology for engineered nanomaterials. Nat. Protoc.

Demokritou, P., Lee, S.J., Ferguson, S.T., Koutrakis, P., 2004. A compact multistage (cascade) impactor for the characterization of atmospheric' aerosols. J. Aerosol Sci. 35, 281–299. https://doi.org/10.1016/j.jaerosci.2003.09.003.

Dobin, A., Davis, C.A., Schlesinger, F., Drenkow, J., Zaleski, C., Jha, S., Batut, P., Chaisson, M., Gingeras, T.R., 2013. STAR: ultrafast universal RNA-seq aligner. Bioinformatics 29, 15–21. https://doi.org/10.1093/bioinformatics/bts635.

Duncan, T.V., 2015. Release of engineered nanomaterials from polymer nanocomposites: the effect of matrix degradation. ACS Appl. Mater. Interfaces 7, 20–39.

Eleftheriadou, M., Pyrgiotakis, G., Demokritou, P., 2017. Nanotechnology to the rescue: using nano-enabled approaches in microbiological food safety and quality. Curr. Opin. Biotechnol. 44, 87–93. https://doi.org/10.1016/j.copbio.2016.11.012.

Gao, T., Sandberg, L.I.C., Jelle, B.P., 2014. Nano insulation materials: Synthesis and life cycle assessment. Procedia CIRP 15, 490–495. https://doi.org/10.1016/j.procir.2014.06.041.

Golanski, L., Gaborieau, A., Guiot, A., Uzu, G., Chatenet, J., Tardif, F., H.L, Vorbau, S.M., M, G.L, Guiot, T.F., A, G.A, Tardif, G.L., F, G.A, Golanski, T.F., L, 2011. Characterization of abrasion-induced nanoparticle release from paints into liquids and air. J. Phys. Conf. Ser. 304, 012062 https://doi.org/10.1088/1742-6596/304/1/012062.

Gomez, V., Levin, M., Saber, A.T., Irusta, S., Maso, M.D., Hanoi, R., Santamaria, J., Jensen, K.A., Wallin, H., Koponen, I.K., 2014. Comparison of dust release from epoxy and paint nanocomposites and conventional products during sanding and sawing. Ann. Occup. Hyg. 58, 983–994. https://doi.org/10.1093/annhyg/meu046.

Grassian, V.H., Haes, A.J., Mudunkotuwa, I.A., Demokritou, P., Kane, A.B., Murphy, C.J., Hutchison, J.E., Isaacs, J.A., Jun, Y.-S., Karn, B., Khondaker, S.I., Larsen, S.C., Lau, B. L.T., Pettibone, J.M., Sadik, O.A., Saleh, N.B., Teague, C., 2016. NanoEHS – defining fundamental science needs: no easy feat when the simple itself is complex. Environ. Sci. Nano 3, 15–27. https://doi.org/10.1039/C5EN00112A.

Guo, N.L., Bello, D., Ye, Q., Tagett, R., Chanetsa, L., Singh, D., Poh, T.Y., Setyawati, M.I., Chotirmall, S.H., Ng, K.W., Demokritou, P., 2020. Pilot deep RNA sequencing of worker blood samples from Singapore printing industry for occupational risk assessment. NanoImpact 19. https://doi.org/10.1016/j.impact.2020.100248.

Guo, N.L., Poh, T.Y., Pirela, S., Farcas, M.T., Chotirmall, S.H., Tham, W.K., Adav, S.S., Ye, Q., Wei, Y., Shen, S., Christiani, D.C., Ng, K.W., Thomas, T., Qian, Y., Demokritou, P., 2019. Integrated transcriptomics, metabolomics, and lipidomics profiling in rat lung, blood, and serum for assessment of laser printer-emitted nanoparticle inhalation exposure-induced disease risks. IJMS 20, 6348. https://doi.org/10.3390/ijms20246348.

Gustafsson, Å., Bergström, U., Ågren, L., Österlund, L., Sandström, T., Bucht, A., 2015. Differential cellular responses in healthy mice and in mice with established airway inflammation when exposed to hematite nanoparticles. Toxicol. Appl. Pharmacol. 288, 1–11.

Han, Z., Fina, A., Camino, G., 2014. Organosilicon Compounds as Polymer Fire Retardants. In: Polymer Green Flame Retard. Elsevier Inc, pp. 389–418. https://doi.org/10.1016/B978-0-444-53808-6.00012-3.

Han, C., Zhao, A., Varughese, E., Sahle-Demessie, E., 2018. Evaluating weathering of food packaging polyethylene-nano-clay composites: release of nanoparticles and their impacts. NanoImpact 9, 61–71. https://doi.org/10.1016/j.impact.2017.10.005.

Hayashi, C., Kashu, S., Oda, M., Naruse, F., 1993. The use of nanoparticles as coatings. Mater. Sci. Eng. A. 163, 157–161. https://doi.org/10.1016/0921-5093(93)90781-9.

L. Hodson, C. Geraci, P. Schulte, Continuing to protect the nanotechnology workforce: NIOSH nanotechnology research plan for 2018 - 2025., 2019. https://doi.org/10.26616/NIOSHPUB2019116.

Hofmann, T., Ma-Hock, L., Strauss, V., Treumann, S., Rey Moreno, M., Neubauer, N., Wohlleben, W., Gröters, S., Wiench, K., Veith, U., Teubner, W., van Ravenzwaay, B., Landsiedel, R., 2016. Comparative short-term inhalation toxicity of five organic diketopyrrolopyrrole pigments and two inorganic iron-oxide-based pigments. Inhal. Toxicol. 28, 463–479. https://doi.org/10.1080/08958378.2016.1200698.

Huggett, C., Levin, B.C., 1987. Toxicity of the pyrolysis and combustion products of poly (vinyl chlorides): A literature assessment. Fire Mater. 11, 131–142. https://doi.org/10.1002/fam.810110303.

Jacobs, D.S., Huang, S.R., Cheng, Y.L., Rabb, S.A., Gorham, J.M., Krommenhoek, P.J., Yu, L.L., Nguyen, T., Sung, L., 2016. Surface degradation and nanoparticle release of a commercial nanosilica/polyurethane coating under UV exposure. J. Coat. Technol. Res. 13, 735–751. https://doi.org/10.1007/s11998-016-9796-2.

Jones, W., Gibb, A., Goodier, C., Bust, P., Song, M., Jin, J., 2016. Nanomaterials in construction – what is being used, and where? Proc. Inst. Civ. Eng. - Constr. Mater. 1–14. https://doi.org/10.1680/jcoma.16.00011.

Kaiser, J.-P., Diener, L., Wick, P., 2013. Nanoparticles in paints: A new strategy to protect façades and surfaces? J. Phys.: Conf. Ser. 429, 012036 https://doi.org/10.1088/1742-6596/429/1/012036.

Kang, J., Erdely, A., Afshari, A., Casuccio, G., Bunker, K., Lersch, T., Dahm, M.M., Farcas, D., Cena, L., 2017. Generation and characterization of aerosols released from sanding composite nanomaterials containing carbon nanotubes. NanoImpact 5, 41–50. https://doi.org/10.1016/j.impact.2016.12.006.

Kan, M., Shumyatcher, M., Diwadkar, A., Soliman, G., Himes, B.E., 2018. Integration of Transcriptomic Data Identifies Global and Cell-Specific Asthma-Related Gene Expression Signatures. AMIA. Annu. Symp. Proc. AMIA Symp. 2018, 1338–1347. ⟨https://github.com/HimesGroup/raved⟩ (accessed April 21, 2021).

Keane, M.P., Arenberg, D.A., Lynch, J.P., Whyte, R.I., Iannettoni, M.D., Burdick, M.D., Wilke, C.A., Morris, S.B., Glass, M.C., DiGiovine, B., Kunkel, S.L., Strieter, R.M., 1997. The CXC chemokines, IL-8 and IP-10, regulate angiogenic activity in idiopathic pulmonary fibrosis. J. Immunol. 159, 1437–1443.

Kermani, M., Jafari, A.J., Gholami, M., Arfaeinia, H., Shahsavani, A., Fanaei, F., 2021. Characterization, possible sources and health risk assessment of PM2.5-bound heavy metals in the most industrial city of Iran. J. Environ. Heal. Sci. Eng. 19, 151–163. https://doi.org/10.1007/S40201-020-00589-3.

Kohga, M., Togo, S., 2020. Catalytic effect of added Fe2O3 amount on thermal decomposition behaviors and burning characteristics of ammonium nitrate/ammonium perchlorate propellants. Combust. Sci. Technol. 192, 1668–1681. https://doi.org/10.1080/00102202.2019.1620736.

Koivisto, A.J., Jensen, A.C.Ø., Kling, K.I., Nørgaard, A., Brinch, A., Christensen, F., Jensen, K.A., 2017. Quantitative material releases from products and articles containing manufactured nanomaterials: towards a release library. NanoImpact 5, 119–132. https://doi.org/10.1016/j.impact.2017.02.001.

Koponen, I.K., Jensen, K.A., Schneider, T., 2011. Comparison of dust released from sanding conventional and nanoparticle-doped wall and wood coatings. J. Expo. Sci. Environ. Epidemiol. 21, 408–418. https://doi.org/10.1038/jes.2010.32.

Lee, J., Mahendra, S., Alvarez, P.J.J., 2010. Nanomaterials in the construction industry: A review of their applications and environmental health and safety considerations. ACS Nano 4, 3580–3590. https://doi.org/10.1021/nn100866w.

Li, H.Y., Gao, P.P., Ni, H.G., 2019. Emission characteristics of parent and halogenated PAHs in simulated municipal solid waste incineration. Sci. Total Environ. 665, 11–17. https://doi.org/10.1016/j.scitotenv.2019.02.002.

Lloyd, C., 2002. Chemokines in allergic lung inflammation. Immunology 105, 144–154. https://doi.org/10.1046/j.1365-2567.2002.01344.x.

Love, M.I., Huber, W., Anders, S., 2014. Moderated estimation of fold change and dispersion for RNA-seq data with DESeq2. Genome Biol. 15, 550. https://doi.org/10.1186/s13059-014-0550-8.

Luster, A.D., Greenberg, S.M., Leder, P., 1995. The IP-10 chemokine binds to a specific cell surface heparan sulfate site shared with platelet factor 4 and inhibits endothelial cell proliferation. J. Exp. Med. 182, 219–231. https://doi.org/10.1084/jem.182.1.219.

Lux Research, Nanotechnology Update: Corporations Up Their Spending as Revenues for Nano-enabled Products Increase, 2014.

Madras, G., Smith, J.M., McCoy, B.J., 1996. Thermal degradation of poly (α-methylstyrene) in solution. Polym. Degrad. Stab. 52, 349–358. https://doi.org/10.1016/0141-3910(95)00242-1.

Mahinroosta, M., 2013. Catalytic effect of commercial nano-CuO and nano-Fe2O3 on thermal decomposition of ammonium perchlorate. J. Nanostruct. Chem. 3, 47. https://doi.org/10.1186/2193-8865-3-47.

Martinez, H., Ren, N., Matta, M.E., Hillmyer, M.A., 2014. Ring-opening metathesis polymerization of 8-membered cyclic olefins. Polym. Chem. 5, 3507–3532. https://doi.org/10.1039/c3py01787g.

Miller, F.J., Asgharian, B., Schroeter, J.D., Price, O., 2016. Improvements and additions to the Multiple Path Particle Dosimetry model. J. Aerosol Sci. 99, 14–26. https://doi.org/10.1016/J.JAEROSCI.2016.01.018.

Mishra, M., Chun, D.M., 2015. α-Fe2O3 as a photocatalytic material: a review. Appl. Catal. A Gen. 498, 126–141. https://doi.org/10.1016/j.apcata.2015.03.023.

Morgan, D.L., Mahler, J.F., Kirkpatrick, D.T., Price, H.C., O'Connor, R.W., Wilson, R.E., Moorman, M.P., 1999. Characterization of inhaled α-methylstyrene vapor toxicity for B6C3F1 mice and F344 rats. Toxicol. Sci. 47, 187–194. https://doi.org/10.1093/toxsci/47.2.187.

Mosurkal, R., Samuelson, L.A., Smith, K.D., Westmoreland, P.R., Parmar, V.S., Yan, F., Kumar, J., Watterson, A.C., 2008. Nanocomposites of TiO2 and siloxane copolymers as environmentally safe flame-retardant materials. J. Macromol. Sci. Part A. 45, 942–946. https://doi.org/10.1080/10601320802380208.

Neubauer, N., Wohlleben, W., Tomović, Ž., 2017. Conductive plastics: comparing alternative nanotechnologies by performance and life cycle release probability. J. Nanopart. Res 19, 112. https://doi.org/10.1007/s11051-017-3817-7.

Oliveira, P.A., Colaço, A., Chaves, R., Guedes-Pinto, H., De-La-Cruz, L.F.P., Lopes, C., 2007. Chemical carcinogenesis. . Acad. Bras. Cienc. 79, 593–916. https://doi.org/10.1590/s0001-37652007000400004.

Pagnin, L., Calvini, R., Wiesinger, R., Weber, J., Schreiner, M., 2020. Photodegradation kinetics of alkyd paints: the influence of varying amounts of inorganic pigments on the stability of the synthetic binder. Front. Mater. 7 https://doi.org/10.3389/fmats.2020.600887.

Pal, A.K., Watson, C.Y., Pirela, S.V., Singh, D., Chalbot, M.C.G., Kavouras, I., Demokritou, P., 2015. Linking exposures of particles released from nano-enabled products to toxicology: An integrated methodology for particle sampling, extraction, dispersion, and dosing. Toxicol. Sci. 146, 321–333. https://doi.org/10.1093/toxsci/kfv095.

Park, E.-J., Kim, H., Kim, Y., Yi, J., Choi, K., Park, K., 2010. Inflammatory responses may be induced by a single intratracheal instillation of iron nanoparticles in mice. Toxicology 275, 65–71.

Park, E.-J., Oh, S.Y., Lee, S.J., Lee, K., Kim, Y., Lee, B.-S., Kim, J.S., 2015. Chronic pulmonary accumulation of iron oxide nanoparticles induced Th1-type immune response stimulating the function of antigen-presenting cells. Environ. Res. 143, 138–147.

Pintus, V., Wei, S., Schreiner, M., 2016. Accelerated UV ageing studies of acrylic, alkyd, and polyvinyl acetate paints: Influence of inorganic pigments. Microchem. J. 124, 949–961. https://doi.org/10.1016/j.microc.2015.07.009.

Pirela, S.V., Martin, J., Bello, D., Demokritou, P., 2017. Nanoparticle exposures from nano-enabled toner-based printing equipment and human health: state of science and future research needs. Crit. Rev. Toxicol. 1–27. https://doi.org/10.1080/10408444.2017.1318354.

Pirela, S.V., Sotiriou, G.A., Bello, D., Shafer, M., Bunker, K.L., Castranova, V., Thomas, T., Demokritou, P., 2015. Consumer exposures to laser printer-emitted engineered nanoparticles: a case study of life-cycle implications from nano-enabled products. Nanotoxicology 9, 760–768. https://doi.org/10.3109/17435390.2014.976602.

Pyrgiotakis, G., Vedantam, P., Cirenza, C., McDevitt, J., Eleftheriadou, M., Leonard, S.S., Demokritou, P., 2016. Optimization of a nanotechnology based antimicrobial platform for food safety applications using Engineered Water Nanostructures (EWNS). Sci. Rep. 6, 21073. https://doi.org/10.1038/srep21073.

Rostam, N.G., Mahdavinejad, M.J., Rostam, M.G., 2015. Commercializing usage of nano-insulating materials in building industry and future architecture. Procedia Mater. Sci. 11, 644–648. https://doi.org/10.1016/j.mspro.2015.11.004.

Saba, N., Tahir, P., Jawaid, M., 2014. A review on potentiality of nano filler/natural fiber filled polymer hybrid composites. In: Polymers (Basel), 6, pp. 2247–2273. https://doi.org/10.3390/polym6082247.

Sadeghi, L., Espanani, H.R., 2015. Toxic effects of the Fe2O3 nanoparticles on the liver and lung tissue. Bratisl. Lek. Listy 116, 373–378.

Santosh, B.S., Madhavi, T.P., 2015. Nanomaterials-application and techniques in civil engineering. J. Civ. Eng. Environ. Technol. 2, 456–460.

Schulte, P.A., Kuempel, E.D., Drew, N.M., 2018. Characterizing risk assessments for the development of occupational exposure limits for engineered nanomaterials. Regul. Toxicol. Pharmacol. 95, 207–219. https://doi.org/10.1016/j.yrtph.2018.03.018.

Singh, D., Schifman, L.A., Watson-Wright, C., Sotiriou, G.A., Oyanedel-Craver, V., Wohlleben, W., Demokritou, P., 2017. Nanofiller presence enhances polycyclic aromatic hydrocarbon (PAH) profile on nanoparticles released during thermal decomposition of nano-enabled thermoplastics: potential environmental health implications. Environ. Sci. Technol. 51, 5222–5232. https://doi.org/10.1021/acs.est.6b06448.

Singh, D., Sotiriou, G.A., Zhang, F., Mead, J., Bello, D., Wohlleben, W., Demokritou, P., 2016. End-of-life thermal decomposition of nano-enabled polymers: effect of nanofiller-loading and polymer matrix on byproducts. Environ. Sci. Nano 3, 1293–1305. https://doi.org/10.1039/C6EN00252H.

Singh, D., Wohlleben, W., De La Torre Roche, R., White, J.C.J.C., Demokritou, P., 2019a. Thermal decomposition/incineration of nano-enabled coatings and effects of nanofiller/matrix properties and operational conditions on byproduct release dynamics: potential environmental health implications. NanoImpact 13, 44–55. https://doi.org/10.1016/J.IMPACT.2018.12.003.

Singh, D., Wohlleben, W., De La Torre Roche, R., White, J.C., Demokritou, P., 2019. Biogenic synthesis and thermo-magnetic study of highly porous carbon nanotubes. IET Nanobiotechnol. 13, 363–367. https://doi.org/10.1016/j.impact.2018.12.003.

Sotiriou, G.A., Singh, D., Zhang, F., Chalbot, M.C.G., Spielman-Sun, E., Hoering, L., Kavouras, I.G., Lowry, G.V., Wohlleben, W., Demokritou, P., 2016. Thermal decomposition of nano-enabled thermoplastics: possible environmental health and safety implications. J. Hazard. Mater. 305, 87–95. https://doi.org/10.1016/j.jhazmat.2015.11.001.

Sotiriou, G.A., Singh, D., Zhang, F., Wohlleben, W., Chalbot, M.-C.G., Kavouras, I.G., Demokritou, P., 2015. An integrated methodology for the assessment of

environmental health implications during thermal decomposition of nano-enabled products. Environ. Sci. Nano 2, 262–272. https://doi.org/10.1039/C4EN00210E.
Srinivas, A., Rao, P.J., Selvam, G., Goparaju, A., Murthy, B.P., Reddy, N.P., 2012. Oxidative stress and inflammatory responses of rat following acute inhalation exposure to iron oxide nanoparticles. Hum. Exp. Toxicol. 31, 1113–1131.
Stratmann, H., Hellmund, M., Veith, U., End, N., Teubner, W., 2020. Indicators for lack of systemic availability of organic pigments. Regul. Toxicol. Pharmacol. 115, 104719 https://doi.org/10.1016/j.yrtph.2020.104719.
Subramanian, A., Tamayo, P., Mootha, V.K., Mukherjee, S., Ebert, B.L., Gillette, M.A., Paulovich, A., Pomeroy, S.L., Golub, T.R., Lander, E.S., Mesirov, J.P., 2005. Gene set enrichment analysis: a knowledge-based approach for interpreting genome-wide expression profiles. Proc. Natl. Acad. Sci. 102, 15545–15550. https://doi.org/10.1073/pnas.0506580102.
Sung, L., Stanley, D., Gorham, J.M., Rabb, S., Gu, X., Yu, L.L., Nguyen, T., 2014. A quantitative study of nanoparticle release from nanocoatings exposed to UV radiation. J. Coat. Technol. Res. 12, 121–135. https://doi.org/10.1007/s11998-014-9620-9.
Szalay, B., Tátrai, E., Nyírő, G., Vezér, T., Dura, G., 2012. Potential toxic effects of iron oxide nanoparticles in in vivo and in vitro experiments. J. Appl. Toxicol. 32, 446–453.
Vaze, N., Pyrgiotakis, G., Mena, L., Baumann, R., Demokritou, A., Ericsson, M., Zhang, Y., Bello, D., Eleftheriadou, M., Demokritou, P., 2019. A nano-carrier platform for the targeted delivery of nature-inspired antimicrobials using Engineered water nanostructures for food safety applications. Food Control 96, 365–374. https://doi.org/10.1016/j.foodcont.2018.09.037.
Vejerano, E.P., Holder, A.L., Marr, L.C., 2013. Emissions of polycyclic aromatic hydrocarbons, polychlorinated dibenzo-p-dioxins, and dibenzofurans from incineration of nanomaterials. Environ. Sci. Technol. 47, 4866–4874. https://doi.org/10.1021/es304895z.
Vejerano, E.P., Leon, E.C., Holder, A.L., Marr, L.C., 2014. Characterization of particle emissions and fate of nanomaterials during incineration. Environ. Sci. Nano 1, 133–143. https://doi.org/10.1039/c3en00080j.
Vorbau, M., Hillemann, L., Stintz, M., 2009. Method for the characterization of the abrasion induced nanoparticle release into air from surface coatings. J. Aerosol Sci. 40, 209–217. https://doi.org/10.1016/j.jaerosci.2008.10.006.
Watson-Wright, C., Singh, D., Demokritou, P., 2017. Toxicological implications of released particulate matter during thermal decomposition of nano-enabled thermoplastics. NanoImpact 5, 29–40. https://doi.org/10.1016/j.impact.2016.12.003.
Wohlleben, W., Brill, S., Meier, M.W., Mertler, M., Cox, G., Hirth, S., Von Vacano, B., Strauss, V., Treumann, S., Wiench, K., Ma-Hock, L., Landsiedel, R., 2011. On the lifecycle of nanocomposites: Comparing released fragments and their in-vivo hazards from three release mechanisms and four nanocomposites. Small 7, 2384–2395. https://doi.org/10.1002/smll.201002054.
Wohlleben, W., Kingston, C., Carter, J., Sahle-Demessie, E., Vázquez-Campos, S., Acrey, B., Chen, C.Y., Walton, E., Egenolf, H., Müller, P., Zepp, R., 2017. NanoRelease: pilot interlaboratory comparison of a weathering protocol applied to resilient and labile polymers with and without embedded carbon nanotubes. Carbon N. Y 113, 346–360. https://doi.org/10.1016/j.carbon.2016.11.011.
Wohlleben, W., Neubauer, N., 2016. Quantitative rates of release from weathered nanocomposites are determined across 5 orders of magnitude by the matrix, modulated by the embedded nanomaterial. NanoImpact 1, 39–45. https://doi.org/10.1016/j.impact.2016.01.001.
Xu, T., Ma, C., Aytac, Z., Hu, X., Ng, K.W., White, J.C., Demokritou, P., 2020. Enhancing agrichemical delivery and seedling development with biodegradable, tunable, biopolymer-based nanofiber seed coatings. ACS Sustain. Chem. Eng. 8, 9537–9548. https://doi.org/10.1021/acssuschemeng.0c02696.
Yates-Binder, C.C., Rodgers, M., Jaynes, J., Wells, A., Bodnar, R.J., Turner, T., 2012. An IP-10 (CXCL10)-derived peptide inhibits angiogenesis. PLoS One 7, 40812. https://doi.org/10.1371/journal.pone.0040812.
Yousif, E., Haddad, R., 2013. Photodegradation and photostabilization of polymers, especially polystyrene: Review. Springerplus 2, 398. https://doi.org/10.1186/2193-1801-2-398.
Zeng, W., Zhou, Q., Zhang, H., Qi, X., 2018. One-coat epoxy coating development for the improvement of UV stability by DPP pigments. Dye. Pigment. 151, 157–164. https://doi.org/10.1016/j.dyepig.2017.12.058.
Zepp, R., Ruggiero, E., Acrey, B., Acrey, B., Davis, M.J.B., Davis, M.J.B., Han, C., Han, C., Han, C., Hsieh, H.S., Hsieh, H.S., Vilsmeier, K., Wohlleben, W., Sahle-Demessie, E., 2020. Fragmentation of polymer nanocomposites: modulation by dry and wet weathering, fractionation, and nanomaterial filler. Environ. Sci. Nano 7, 1742–1758. https://doi.org/10.1039/c9en01360a.
Zhu, M.-T., Feng, W.-Y., Wang, B., Wang, T.-C., Gu, Y.-Q., Wang, M., Wang, Y., Ouyang, H., Zhao, Y.-L., Chai, Z.-F., 2008. Comparative study of pulmonary responses to nano-and submicron-sized ferric oxide in rats. Toxicology 247, 102–111.